Direct Surface Thermodynamic Observations within the Rear-Flank Downdrafts of Nontornadic and Tornadic Supercells

PAUL M. MARKOWSKI

Department of Meteorology, The Pennsylvania State University, University Park, Pennsylvania

JERRY M. STRAKA

School of Meteorology, University of Oklahoma, Norman, Oklahoma

ERIK N. RASMUSSEN

Cooperative Institute for Mesoscale Meteorological Studies, National Severe Storms Laboratory, and University of Oklahoma, Norman, Oklahoma

(Manuscript received 19 March 2001, in final form 7 November 2001)

ABSTRACT

Despite the long-surmised importance of the hook echo and rear-flank downdraft (RFD) in tornadogenesis, only a paucity of direct observations have been obtained at the surface within hook echoes and RFDs. In this paper, in situ surface observations within hook echoes and RFDs are analyzed. These ''mobile mesonet'' data have unprecedented horizontal spatial resolution and were obtained from the Verifications of the Origins of Rotation in Tornadoes Experiment (VORTEX) and additional field experiments conducted since the conclusion of VORTEX. The surface thermodynamic characteristics of hook echoes and RFDs associated with tornadic and nontornadic supercells are investigated to address whether certain types of hook echoes and RFDs are favorable (or unfavorable) for tornadogenesis.

Tornadogenesis is more likely and tornado intensity and longevity increase as the surface buoyancy, potential buoyancy (as measured by the convective available potential energy), and equivalent potential temperature in the RFD increase, and as the convective inhibition associated with RFD parcels at the surface decreases. It is hypothesized that evaporative cooling and entrainment of midlevel potentially cold air may play smaller roles in the development of RFDs associated with tornadic supercells compared to nontornadic supercells. Furthermore, baroclinity at the surface within the hook echo is not a necessary condition for tornadogenesis. It also will be shown that environments characterized by high boundary layer relative humidity (and low cloud base) may be more conducive to RFDs associated with relatively high buoyancy than environments characterized by low boundary layer relative humidity (and high cloud base).

1. Introduction and motivation

No obvious characteristics capable of discriminating between hook echoes associated with tornadic and nontornadic supercells are apparent in radar reflectivity data (Fig. 1). Moreover, recent dual-Doppler radar observations from Verification of the Origins of Rotation in Tornadoes Experiment (VORTEX) have shown that, at least kinematically, the differences between tornadic and nontornadic supercells are subtle, if even distinguishable in three-dimensional velocity data (Blanchard and Straka 1998; Wakimoto and Liu 1998; Wakimoto et al. 1998; Trapp 1999; Wakimoto and Cai 2000). The images in Fig. 1 highlight a major forecasting challenge—how can tornadic supercells be distinguished from nontornadic supercells, let alone their tornado potential be anticipated in advance?

Although the dynamical relationship remains poorly understood, the association among hook echoes, rear-flank downdrafts (RFDs), and tornadoes is well established (Markowski 2002a). However, direct observations within hook echoes and RFDs have been scarce. A few observations have been mentioned by van Tassell (1955), Beebe (1959), Garrett and Rockney (1962), Browning and Ludlam (1962), Charba and Sasaki (1971), Lemon (1976), Barnes (1978a,b), Brown and Knupp (1980), and Bluestein (1983). Thermodynamic retrievals have been performed (e.g., Brandes 1984a; Hane and Ray 1985), but small-scale details cannot be resolved, buoyancy fields often are noisy, and data within the surface layer, which are perhaps most important, are unavailable. Would in situ surface observations col-

Corresponding author address: Dr. Paul Markowski, 503 Walker Building, University Park, PA 16802.
E-mail: marko@mail.meteo.psu.edu

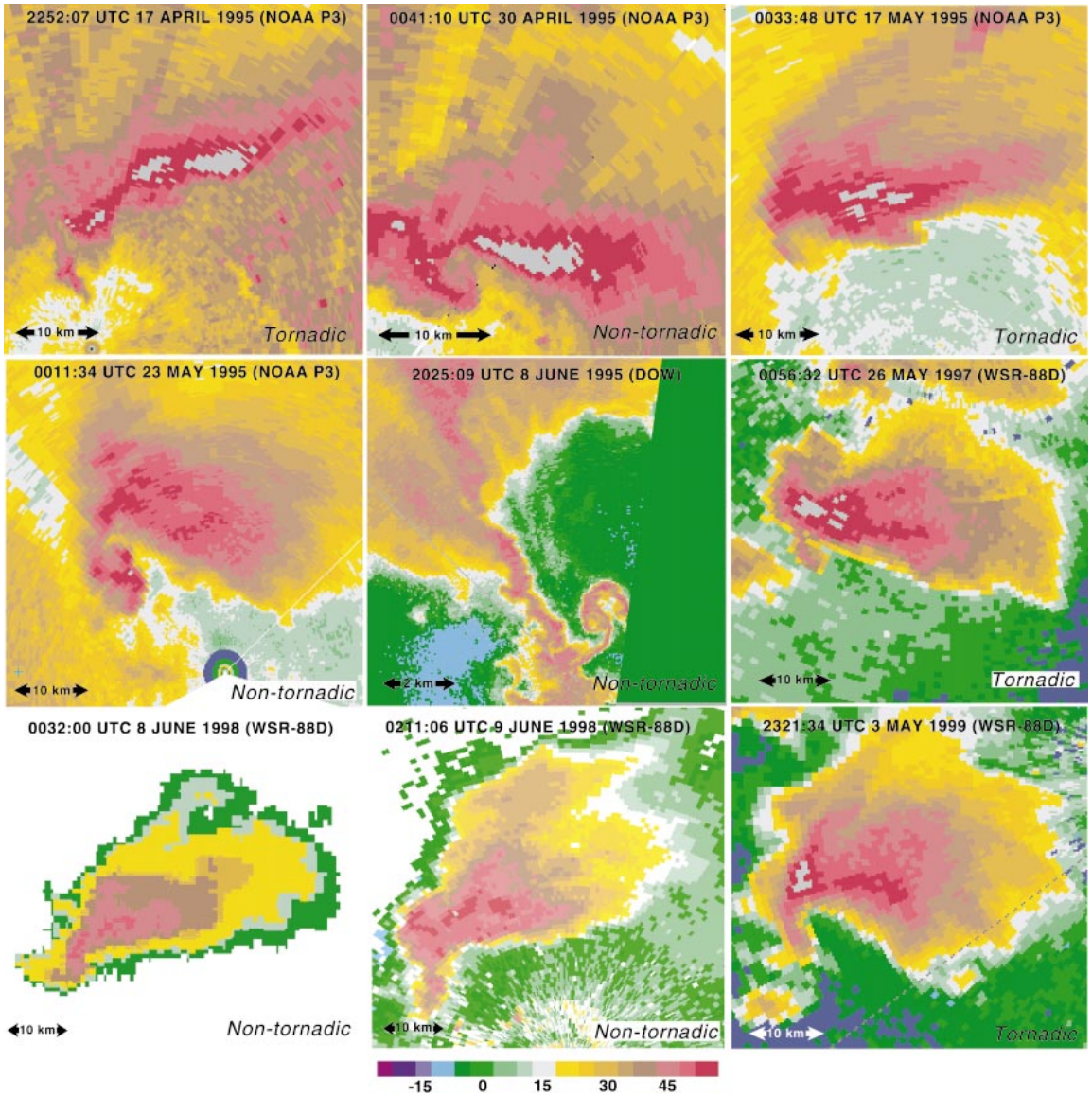

FIG. 1. A sample of some of the hook echoes associated with both tornadic and nontornadic supercells from which mobile mesonet observations have been collected. The hook echoes associated with tornadic supercells are as they appeared 5 min or less prior to tornadogenesis. No obvious, systematic differences are apparent between the hook echoes associated with the tornadic and nontornadic supercells.

lected in the RFDs of the nontornadic and tornadic supercells analyzed by Blanchard and Straka, Wakimoto et al., and Trapp reveal significant differences? And could any differences detected by a mobile mesonet ever be inferred from environmental data available routinely on larger scales?

The ''mobile mesonet'' is an observing system comprising vehicle-borne sensors that provide direct measurements of temperature, moisture, wind velocity, and pressure (Straka et al. 1996). The observing platform was developed for VORTEX (Rasmussen et al. 1994) and has been heavily relied upon in smaller subsequent storm intercept projects organized by the National Severe Storms Laboratory and University of Oklahoma. In this paper, 5 years of observations of nontornadic and tornadic supercell RFD and hook echo regions are summarized. The paper has two main objectives: 1) document the surface thermodynamic fields in the proximity of tornadic and nontornadic mesocyclones at a resolution not previously possible; 2) determine if differences exist at the surface in the hook echoes and RFDs of tornadic and nontornadic supercells.

a. Documentation of surface thermodynamic fields

Brandes (1984a) and Hane and Ray (1985) were among the first to use the pioneering methods proposed by Gal-Chen (1978) and Hane et al. (1981) to retrieve

thermodynamic (buoyancy and pressure) fields in supercells from multiple-Doppler-radar-synthesized three-dimensional wind fields. However, the computation of buoyancy requires assumptions about lateral boundary conditions and the forcing for buoyancy involves one more derivative than the forcing for pressure. Thus, buoyancy fields retrieved in past studies may contain significant uncertainties and usually contain greater noise than retrieved pressure fields.

The spatial resolution of retrieval results is limited by the resolution of the dual–Doppler radar data. Usually horizontal resolution is limited to 1–3 km. Furthermore, ground clutter contaminates Doppler velocities; therefore, thermodynamic variables typically cannot be reliably retrieved at altitudes less than about 500 m above ground level (AGL). (In some cases, a height of 500 m AGL may be within the cloud.) Although radars can provide three-dimensional observations of entire storms (something that an observing system of vehicle-borne instruments cannot do), they cannot sample the surface layer, which surely must be one of the most critical regions within a storm. By definition, a tornado is a phenomenon *rooted in the surface layer*. We contend that direct measurements of surface conditions may be some of the most important observations for investigators attempting to address questions pertaining to tornadogenesis.

Some might argue that observations are unnecessary because computing power now has increased to a level such that three-dimensional numerical simulations of supercells can be conducted with a horizontal and vertical resolution of less than 250 m (especially if grid nesting is employed). However, important processes must unavoidably be parameterized (e.g., microphysics and subgrid-scale mixing). Microphysics plays a critical role in dictating the degree of evaporational cooling within simulated storms; thus, surface thermodynamic fields are sensitive to microphysics parameterizations. Numerical simulations almost invariably have produced cold RFDs [temperature deficits >5 K; e.g., Klemp and Rotunno (1983); Rotunno and Klemp (1985); Wicker and Wilhelmson (1995); Adlerman et al. (1999)],[1] at least partly because the exclusion of ice leads to more concentrated downdrafts. The inclusion of ice leads to the distribution of hydrometeors over a larger horizontal region and a reduction of the outflow intensity in close proximity to the updraft (Johnson et al. 1993). Some past observations (e.g., Fujita et al. 1977; Brown and Knupp 1980; Bluestein 1983; Rasmussen and Straka 1996), as well as those that will be presented herein, reveal that the RFDs associated with many strong tornadoes are relatively warm, both in terms of temperature and equivalent potential temperature.

b. *Differences between tornadic and nontornadic supercells*

Many studies have found that the air parcels that enter the tornado pass through the RFD. For example, observations by Brandes (1978), Lemon and Doswell (1979), Rasmussen et al. (1982), and Jensen et al. (1983) have shown or implied a near-total occlusion of the low-level mesocyclone by the RFD prior to tornadogenesis. Furthermore, Wicker and Wilhelmson (1995) found that trajectories entering their simulated tornado-like vortex passed through the hook echo and RFD. Recent tornadogenesis hypotheses [e.g., those proposed by Davies-Jones and Brooks (1993) and Rasmussen and Straka (1996)[2]] also have depended on air entering the tornado from the RFD. Davies-Jones and Brooks (1993) hypothesized that baroclinic generation of vorticity and reorientation of vortex lines in the RFD and hook echo were prerequisites for tornadogenesis, although the prerequisite of baroclinity within the hook echo recently has been questioned by Davies-Jones (2000) and Markowski et al. (2000).

Given the prior emphasis on the RFD in the tornadogenesis process and the apparent consensus that RFD air parcels enter the tornado, the buoyancy and buoyancy gradients in hook echoes and RFDs naturally assume importance. Leslie and Smith (1978) presented results from idealized numerical simulations that indicated the generation of intense surface vorticity could be precluded if low-level stability was too strong. Furthermore, Brooks et al. (1993, 1994a) showed that the cold air to the rear of numerically simulated supercell updrafts could undercut the mesocyclone and preclude generation of strong low-level rotation in some ''failure cases.'' And it is worth noting Ludlam's (1963) hypothesis: ''if (the RFD) contains the potentially cold air from middle levels its ascent (into the tornado and parent updraft) might be expected to impede if not destroy the tornado . . . *it may be particularly important for the intensification and persistence of a tornado that some of the downdraft air be derived from potentially warm air* . . ..'' Can tornadogenesis occur only for special ranges of buoyancy and/or buoyancy gradients within hook echoes and RFDs?

2. Data description and analysis techniques

Mobile mesonet data from 24 days from 1994 to 1999 were analyzed. Included in this sample are 30 hook

[1] Some recent exceptions include simulations of supercells occurring in landfalling hurricane environments, in which temperature deficits of only 3–5 K have been reported in the downdrafts (McCaul and Weisman 1996), as well as simulations in which the environment has relatively small potential buoyant energy and a large low-level relative humidity (McCaul and Weisman 2001).

[2] Presented orally at the Severe Local Storms Conference in San Francisco, California, sponsored by the American Meteorological Society.

TABLE 1. Cases of mobile mesonet observations obtained within the hook echoes and RFDs of nontornadic supercells. All times are UTC. The date given for each case is with respect to local, not UTC, time.

Case	Date	Location	Time of max rotational velocity (max rotational velocity) on WSR-88D 0.5° tilt	Height of 0.5° tilt (km ARL)	WSR-88D data available	Sounding used in conjunction with the mobile mesonet data
1	29 May 1994	Loving, TX	2252:07 (32 m s^{-1})	2.4	KFWS	Springtown, TX (2204 UTC)
2	29 Apr 1995	Sherman, TX	0028:32 (25 m s^{-1})	2.4	KFWS	Gainesville, TX (2205 UTC)
3	12 May 1995	Hays, KS	2311:39 (42 m s^{-1})	3.5	KDDC	Hays, KS (2206 UTC)
4	22 May 1995	Shamrock, TX	0013:20 (21 m s^{-1})	2.3	KAMA	Lutie, TX (0059 UTC)
5	8 Jun 1995	Elmwood, OK	2014:43 (14 m s^{-1})	2.3	KDDC	Follett, TX (2024 UTC)
6	19 May 1998	Sidney, NE	0205:12 (12 m s^{-1})	2.9	KCYS	North Platte, NE (0000 UTC)
7	20 May 1998	Yuma, CO	0145:33 (15 m s^{-1})	1.5	KGLD	North Platte, NE (0000 UTC)
8	24 May 1998	Medicine Lodge, KS	0126:05 (29 m s^{-1})	1.6	KICT	Norman, OK (0000 UTC)
9	8 Jun 1998	Oklahoma City, OK	0211:06 (19 m s^{-1})	0.3	KTLX	Norman, OK (0000 UTC)
10	9 Jun 1998	Seymour, TX	2134:00 (19 m s^{-1})	0.7	KFDR	Fort Worth, TX (0000 UTC)
11	26 May 1999	Carlsbad, NM	2151:08 (18 m s^{-1})	4.8	KMAF	Seminole, TX (1912 UTC)
12	26 May 1999	Mentone, TX	0056:00 (20 m s^{-1})	2.5	KMAF	Midland, TX (0000 UTC)

echoes[3] in tornadic and nontornadic supercells [Tables 1 and 2; hook echoes associated with more than one tornado (or at least in the radar data, only a single hook echo evolution was observed to be associated with multiple tornadoes) were counted as single cases]. Tornadoes were associated with the hook echoes and RFDs in 18 cases, and of the 12 nontornadic cases, circulations were observed at the surface in all but 1 case [8 June 1998—a mesocyclone[4] was detected by the Weather Surveillance Radar-1988 Doppler (WSR-88D) at an elevation of 300 m above radar level (ARL)]. The tornadic cases included tornadoes of all intensities, ranging from F0 to F5. The 1994 and 1995 cases were from VORTEX operations days. On these days, radar data from the National Oceanic and Atmospheric Administration (NOAA-P3) lower fuselage and tail radars, and occasionally from ground-based mobile Doppler radars, were used in the analyses. For the cases during 1997–99, WSR-88D data were used in the analyses.

Throughout this paper, we will refer to the RFD as *the contiguous downdraft region that surrounds the low-level mesocyclone or tornado.* While it is probable that different parts of the RFD may have different dominant forcings at different times, in the mobile mesonet observations and visual observations in the field, the downdraft has the appearance of a single entity (e.g., only one ''clear slot'' is visible). We will not attempt to discriminate between what Klemp and Rotunno (1983) called an ''occlusion downdraft'' and the major downdraft on the rear flank of supercells, originally identified by Browning and Ludlam (1962), and later referred to as the RFD.

[3] The following criterion for classification of an echo as a ''hook echo'' has been adopted from Forbes (1981): an appendage with echo protrusion oriented at least 60° to the right (typically south) of the main echo movement.

[4] ''Mesocyclone'' is defined throughout as a region where the horizontal shear exceeded 5×10^{-3} s^{-1} in radar radial velocity data.

a. Mobile mesonet data

1) INSTRUMENT SPECIFICATIONS AND QUALITY CONTROL PROCEDURES

The mobile mesonet samples storms with high spatial (100–1000 m) and temporal (10–60 s) resolutions. The variables recorded include time and position [both using a global positioning system (GPS) receiver], ''fast'' temperature (measured by a short-response thermistor), ''slow'' temperature (measured with a slower response time, comparable to the response time of the relative humidity sensor, so that derived quantities that are functions of temperature and moisture can be accurately computed, e.g., dewpoint temperature), relative humidity, pressure, and wind velocity. Data were recorded at 2-s intervals during the years of this study. Additional technical specifications (such as instrument errors and response times) are provided by Straka et al. (1996). In the appendix, the errors of the derived quantities analyzed in this paper are investigated.

Numerous quality control tests were performed on the data prior to analysis:

Radio frequency interference: Field operations required fairly frequent use of a 40-W VHF transceiver, as well as other communication equipment. Use of these transmitters caused large errors in several meteorological quantities. The source for these errors was believed to be radio frequency (RF) interference: when large RF energy was present, the flux gate compass produced large voltages that overwhelmed the datalogger and corrupted the data. Data collected when RF interference was detected (the flux gate compass output was used as a detector of this interference) were not included in the analyses.

Position: Occasionally vehicle position estimates did not update for short intervals, causing erroneous

TABLE 2. Cases of mobile mesonet observations obtained within the hook echoes and RFDs of tornadic supercells. All times are UTC. For TVS types, ND (D) indicates nondescending (descending) TVS, following the criteria of Trapp et al. (1999) (N/A means that either no TVS was detected or level II WSR-88D data were unavailable). The date given for each case is with respect to local, not UTC, time.

Case	Date	Location	Tornado times	Duration (min)	Fujita rating	Estimated max diameter (m)	TVS type	WSR-SSD data available	Sounding data used in conjunction with the mobile mesonet data
13	6 May 1994	Kaw Lake, OK	0012–0023	11	F1	100	D	KINX	Pawnee, OK (2229 UTC)
14	25 May 1994	Northfield, TX	2230–2300	30	F3	500	D	KLBB	Lubbock, TX (2300 UTC)
15	17 Apr 1995	Temple, OK	2256–2300	4	F1	50	N/A	KTLX	Bowie, TX (2200 UTC)
16	16 May 1995	Jetmore, KS	0049–0054	5	F0	<50	N/A	KDDC	Dodge City, KS (2339 UTC)
17	16 May 1995	Hanston, KS	0138–0230	44	F3	500	ND	KDDC	Hanston, KS (0208 UTC)
18	2 Jun 1995	Friona, TX	2343–0015	32	F4	500	N/A	KLBB	Aiken, TX (2248 UTC)
19	2 Jun 1995	Dimmitt, TX	0057–0118	21	F4	275	N/A	KLBB	Dimmitt, TX (0110 UTC)
20	8 Jun 1995	Wheeler, TX	2335–0030	55	F5	500	N/A	KFDR	Cheyenne, OK (0100 UTC)
21	8 Jun 1995	Allison, TX	0045–0131	46	F4	2000	N/A	KFDR	Cheyenne, OK (0100 UTC)
22	25 May 1997	South Haven, KS	0135–0155	20	F2	1500	D	KICT	Norman, OK (0000 UTC)
23	7 Jun 1998	Farwell, TX	0042	<1	F0	<50	N/A	KFDX	Amarillo, TX (0000 UTC)
24	3 May 1999	Apache, OK	2220–2235	15	F3	100	D	KTLX	Norman, OK (0000 UTC)
25	3 May 1999	Minco, OK	0047–0100	13	F1	60	D	KTLX	Norman, OK (0000 UTC)
26	20 May 1999	Jericho, TX	2313–2315	2	F0	<50	D	KAMA	Memphis, TX (1959 UTC)
27	25 May 1999	Roswell, NM	2125–2132	7	F1	<50	N/A	KLBB	Roswell, NM (2212 UTC)
28	31 May 1999	Sitka, KS	0029–0039	10	F1	150	D	KDDC	Canadian, TX (2018 UTC)
29	1 Jun 1999	Coleman, OK	0006	<1	F0	<50	N/A	KTLX	Okemah, OK (2003 UTC)
30	2 Jun 1999	Nazareth, TX	0045	<1	F0	<50	D	KLBB	Flagg, TX (0011 UTC)

latitude, longitude, and wind velocity. These data were not included in the analyses.

Vehicle heading: Vehicle heading (used to determine wind velocity) was measured by a flux-gate compass when stationary and by GPS when moving. The flux-gate compass measures direction with respect to magnetic north, while GPS directions are relative to true north. Moreover, the magnetic fields induced by the vehicles are an additional error source for the flux-gate compasses. Both sources of errors in vehicle heading were removed prior to analysis.

Wind velocity: Vehicle accelerations (determined using the GPS heading and speed data) can lead to significant errors in the pressure and wind velocity data. If the vehicle velocity changed by >4 m s^{-1} in a 6-s interval, wind velocity data from that interval were excluded from the analysis.

In addition to the above quality control checks, significant biases were removed using vehicle intercomparisons. The intercomparisons involved assembling observations over a period of 30–60 min in relatively quiescent weather conditions, while the vehicles were moving as a caravan. Biases were removed if the intercomparison revealed a bias magnitude >0.2 K for ''fast'' temperature, >0.2 K for ''slow'' temperature, >0.2 mb for pressure, $>10°$ for wind direction, and >1 m s^{-1} for wind speed. If biases were very large (5 times the above magnitudes), it was assumed that instrument performance was unacceptable and the data were excluded from the analysis entirely.

2) TIME-TO-SPACE CONVERSION

Quality-controlled observations used in the analyses usually were averaged over 12-s intervals (occasionally 6-s averaging was employed, if vehicle speeds relative to the storm were large). The data were plotted relative to the radar echoes using time-to-space conversion. In other words, if one could assume that a feature being analyzed did not change its character significantly over the time interval during which measurements were made [the ''Taylor hypothesis''; Taylor (1938)], then assuming the velocity $\mathbf{v} = (u, v)$ of the feature was known at some reference time, t_{ref}, the distance traveled by the feature in time Δt would be $u\Delta t$ in the x direction and $v\Delta t$ in the y direction. Therefore, the reference time coordinates (x', y') of a measurement taken at time $t_{\text{ref}} + \Delta t$ and at location (x, y) are

$$x' = x - u\Delta t \tag{1}$$

$$y' = y - v\Delta t. \tag{2}$$

For most analyses, the maximum allowed $|\Delta t|$ ($|\Delta t_{\max}|$) was 2–3 min; that is, a steady-state assumption was made for approximately the time it takes the WSR-88D to complete a volume scan. At analysis times in which features were evolving rapidly, such that the steady-state assumption could not be made reliably for $\pm$2–3 min, smaller values of $|\Delta t_{\max}|$ (sometimes <1 min) were used.

Whenever possible, analyses were obtained within 5 min of tornadogenesis or the time of strongest rotation on WSR-88D at the lowest (0.5°) elevation angle, defined as the time of ''tornadogenesis failure.'' For some

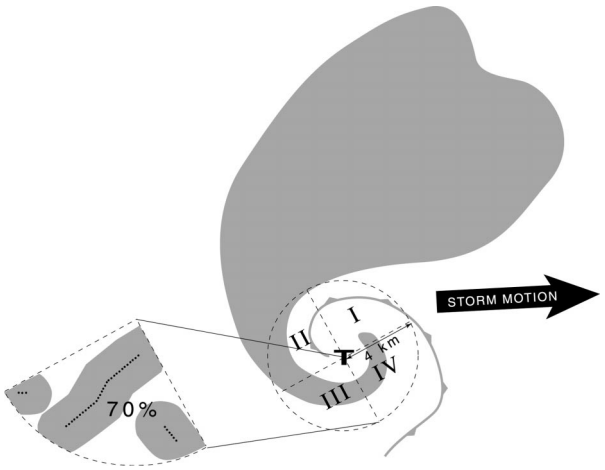

FIG. 2. Schematic illustrating the arbitrarily defined quadrants I, II, III, and IV. In this depiction, 70% of the area of quadrant III is within 1 km of a mobile mesonet observation (denoted by black dots). Similarly, the densities of mobile mesonet observations for each analysis are summarized in Table 3.

cases this was not possible, owing to logistical problems common to data collection in the field; in such cases, the analysis time for which observation density was greatest is shown instead.

3) DENSITY OF MOBILE MESONET OBSERVATIONS

The area sampled within RFDs and hook echoes varied from case to case, owing to logistical limitations inherent in storm intercept field research (e.g., road networks often do not allow observations to be collected in important regions of the thunderstorm). We have attempted to quantify the quality of the RFD sampling in each case by dividing the circulation region (defined as having a radius of 4 km) into four quadrants, I–IV, with the line separating quadrants I and IV from quadrants II and III being parallel to the ''neck'' of the hook echo (Forbes 1978) and passing through the circulation center (Fig. 2). Within each quadrant, the fraction of the area that was within 1 km of a mobile mesonet observation was estimated to the nearest 10%. The fractions for each case are presented in Table 3.

b. Radar data

For the cases analyzed from VORTEX (1994–95), radar data were available from the P3 research aircraft operated by NOAA. The aircraft was equipped with two radars: a lower fuselage (LF) noncoherent radar and a Doppler tail (TA) radar. For detailed descriptions of these radars, the reader is referred to Jorgensen et al. (1983) and Ray et al. (1985).

TABLE 3. Sampling densities by quadrant (Fig. 2) for each of the 30 hook echo cases *at the analysis times* analyzed in section 3 (chosen to be as near as possible to the time of tornadogenesis or tornadogenesis failure). Numerals represent the percent of the area within each quadrant that was within 1 km of a mobile mesonet observation.

Case	Date	Location	Quadrant I	Quadrant II	Quadrant III	Quadrant IV
1	29 May 1994	Loving, TX	0	20	10	20
2	29 Apr 1995	Sherman, TX	90	70	70	80
3	12 May 1995	Hays, KS	50	0	30	10
4	22 May 1995	Shamrock, TX	60	40	80	60
5	8 Jun 1995	Elmwood, OK	10	50	70	70
6	19 May 1998	Sidney, NE	90	50	50	70
7	20 May 1998	Yuma, CO	50	40	60	0
8	24 May 1998	Medicine Lodge, KS	50	20	50	70
9	8 Jun 1998	Oklahoma City, OK	10	0	60	70
10	9 Jun 1998	Seymour, TX	100	40	50	100
11	26 May 1999	Carlsbad, NM	90	40	80	100
12	26 May 1999	Mentone, TX	90	30	80	80
13	6 May 1994	Kaw Lake, OK	100	50	70	80
14	25 May 1994	Northfield, TX	0	0	50	0
15	17 Apr 1995	Temple, OK	90	30	60	90
16	16 May 1995	Jetmore, KS	0	0	30	50
17	16 May 1995	Hanston, KS	100	50	50	0
18	2 Jun 1995	Friona, TX	100	90	10	40
19	2 Jun 1995	Dimmitt, TX	40	90	40	60
20	8 Jun 1995	Wheeler, TX	100	80	40	30
21	8 Jun 1995	Allison, TX	50	70	50	80
22	25 May 1997	South Haven, KS	0	0	20	70
23	7 Jun 1998	Farwell, TX	90	10	70	100
24	3 May 1999	Apache, OK	100	20	30	60
25	3 May 1999	Minco, OK	100	70	20	100
26	20 May 1999	Jericho, TX	10	30	40	70
27	25 May 1999	Roswell, NM	0	50	80	0
28	31 May 1999	Sitka, KS	40	70	50	0
29	1 Jun 1999	Coleman, OK	90	30	20	40
30	2 Jun 1999	Nazareth, TX	90	60	70	80

During VORTEX, the antenna rotation rate of the lower fuselage radar was 2 rpm (Daugherty et al. 1996); lower fuselage radar data were often desirable for analysis with the mobile mesonet data because of the high temporal resolution of these radar data. Constant altitude plan position indicators (CAPPIs) could be constructed from the tail radar data (reflectivity, velocity, and spectrum width), but only at roughly 7-min intervals.

The NOAA-P3 position (obtained from GPS) was saved only at the *beginning* of each scan. If the aircraft was moving at, for example, 120 m s^{-1}, the aircraft would have traveled 3600 m in the time it takes to complete one scan, and significant errors in the locations of the reflectivity data would have been present in the data. To place mobile mesonet observations in the correct positions with respect to LF reflectivity data, WSR-88D images were overlaid atop the LF reflectivity and mobile mesonet data, and the LF reflectivity data were shifted so that the reflectivity cores sampled by the two radars were in phase.[5] Another effect due to the updating of the NOAA-P3 position once per scan is that the shapes of echoes are distorted. However, for the region of the storm of interest (e.g., the hook echo), echoes typically only subtended 10°–20° of azimuth (range ~15–30 km typically). In the time it takes the LF radar to scan 10°–20° (<2 s), the aircraft position only changes by 100–200 m (less than the 250-m gate spacing); thus, echo distortion in the regions of the hook echoes owing to position errors was not severe.

At some of the analysis times for 1995 cases, radar data from the Doppler on Wheels (DOW) radar were superposed. A full description of this 3-cm mobile radar can be obtained from Wurman et al. (1997).

Cases analyzed from 1997 to 1999 generally incorporated WSR-88D archive level II data. For two cases (7 and 9 June 1998), level III data were used. Level II data are the base digital data (mean radial velocity, reflectivity, and spectrum width) produced by the signal processor at the full temporal resolution and nearly the full spatial resolution[6] of the radar. Level III data only include some of the graphic products archived by a radar site on a given day (typically includes base reflectivity and velocity at the lowest two elevation angles).

c. Thermodynamic variables analyzed

Analyses of virtual and equivalent potential temperature, RFD parcel origins (by examining sounding data and using moist entropy as a tracer), potential buoyancy in the RFD as measured by surface-based convective available potential energy (CAPE) and convective inhibition (CIN), and pressure were performed, using the data gathered by the mobile mesonet. For the analyses of virtual and equivalent potential temperature and pressure, the fluctuations of these variable were computed by subtracting a base (''reference'') state value that depended on the large-scale atmospheric conditions (e.g., $p' = p - \overline{p}$, where p is pressure, p' is the pressure fluctuation, and $\overline{p}$ is the base-state pressure). The method by which the base state was determined is described in section 2d. The potential errors of all variables (including derived variables) are analyzed in the appendix.

1) VIRTUAL POTENTIAL TEMPERATURE

A virtual potential temperature, θ_v, is defined here as

$$\theta_v = \theta(1 + 0.61q_v - q_l), \tag{3}$$

where θ is the potential temperature, q_v is the water vapor mixing ratio, and q_l is the liquid water mixing ratio. Ice and cloud water concentrations have been neglected here, and the base state is assumed to contain no hydrometeors. The above definition of θ_v is equivalent to that appearing in the *Glossary of Meteorology* (Glickman 2000) Emanuel (1994), however, refers to the quantity defined by (3) as the density potential temperature, θ_ρ.

Virtual potential temperature fluctuations are proportional to density fluctuations, which appear in the familiar ''buoyancy force.'' However, historically, virtual potential temperature has been favored over the use of density in buoyancy analyses. It can be shown that $g\theta_v'/\overline{\theta}_v$ is equal to the traditional formulation of the buoyancy force involving density (ρ) deviations from a hydrostatic base state, $-g\rho'/\rho$, when the Exner function, π, is used in place of pressure (e.g., Brandes 1984a; Hane and Ray 1985), and when cloud water and ice are neglected. The use of π and θ_v results in part of the p' contribution to ρ' being absorbed by θ_v', and the rest of the p' contribution to ρ' [cf. (2.52) of Houze (1993)] being absorbed by π'.

The liquid water mixing ratio was parameterized using radar reflectivity sampled at the lowest elevation angle obtainable, following Rutledge and Hobbs (1984):

$$q_l(\text{g kg}^{-1}) = 10^{[(z\ -\ 42.2)/16.8]}, \tag{4}$$

where Z is radar reflectivity in dBZ. The reliability of this parameterization is adversely affected by the presence of ice (especially hail). An under- or overestimate of Z by 15 dBZ when measured reflectivity values lie in the 30–45 dBZ range has approximately the same effect on θ_v as a 0.3-K potential temperature fluctuation. The ice mixing ratio has been neglected in the buoyancy computations, although some ice probably is accounted for in the parameterization of q_l in terms of the radar reflectivity factor.

Radar reflectivity factors (dBZ) were objectively an-

[5] Reflectivity core positions were compared because they appeared similar in the data collected by both radars; however, the hook echo regions can appear significantly different when viewed by WSR-88D versus the LF radar at close range.

[6] The signal processor averages the reflectivity data over four gates and thus does not provide reflectivity data at the full spatial resolution of the radar.

alyzed using a one-pass Barnes (1964) scheme with a weight function, w_{ik},

$$w_{ik} = \exp\left(-\frac{x_{ik}^2}{\kappa_x} - \frac{y_{ik}^2}{\kappa_y}\right), \quad (5)$$

where $\kappa = \kappa_x = \kappa_y$ is the ''smoothing parameter,'' and x_{ik} and y_{ik} are the distances of the kth datum from the ith grid point in the x and y directions, respectively. For the NOAA-P3 data, a value of 0.04 km^2 was chosen for κ, which yielded a response of 0.5 at the minimum resolvable wavelength in the (horizontal) direction of worst data resolution (approximately 1 km, assuming four grid points are needed to resolve a wave). For the WSR-88D data, κ was chosen such that the response function was similar; however, the exact value varied from case to case because of widely varying ranges from the radars and, thus, widely varying minimum resolvable scales. The objectively analyzed radar reflectivity data were linearly interpolated to the mobile mesonet observation locations, where q_l and θ_v subsequently were computed.

2) EQUIVALENT POTENTIAL TEMPERATURE

Values of equivalent potential temperature, θ_e, were computed using the formula derived by Bolton (1980):[7]

$$\theta_e = T\left(\frac{p_o}{p}\right)^{0.2854(1-0.28q_v)} \times \exp\left[q_v(1 + 0.81q_v)\left(\frac{3376}{T^*} - 2.54\right)\right], \quad (6)$$

where p_o is a reference pressure equal to 1000 mb and T^* is the temperature, T, at the saturation point (Betts 1982) of the air sample,

$$T^* = \frac{2840}{3.5 \ln T - \ln e - 4.805} + 55, \quad (7)$$

where e is the vapor pressure of the air sample.

Often wet-bulb potential temperature (θ_w) is used in severe thunderstorm studies, because of its similar conservation properly for dry- and moist-adiabatic processes. Bohren and Albrecht (1998, p. 298) showed that

$$\theta_e \approx \theta_w + \frac{L_v}{c_p} q_{vs}; \quad (8)$$

therefore,

$$\theta_e' \approx \theta_w' + \frac{L_v}{c_p} q_{vs}', \quad (9)$$

where L_v is the latent heat of vaporization, c_p is the specific heat of dry air at constant pressure, q_{vs} is the saturation water vapor mixing ratio, and $q_{vs}' = q_{vs}'(T', p')$ is the saturation water vapor mixing ratio fluctuation. For $T \sim 300$ K, $T' \sim 3$ K, and $p' \sim 0$ mb, it can be shown that $q_{vs}' \sim 5$ g kg^{-1} and $\theta_e' - \theta_w' \sim 12$ K.

3) PARCEL ORIGIN

If moist entropy (θ_e) is approximately conserved for adiabatic processes, then it is possible to estimate the height from which surface parcels in the RFD have descended, if the vertical profile of θ_e is available from a nearby sounding. The height of parcel origins (z_o) assuming θ_e conservation (no entrainment) was analyzed for each case. However, z_o values should be viewed with caution, because lateral entrainment clearly must occur in order to satisfy mass continuity if vertical accelerations exist. Furthermore, if parcels reach the surface with the same θ_e as the inflow (and updraft), perhaps via forced descent, then the height from which they have descended cannot be determined, because the updraft has, to a good approximation (at least away from its lateral boundaries), no vertical θ_e gradient. It perhaps is most appropriate to denote z_o as simply the height on an inflow sounding where θ_e values are equal to those observed at the surface within the downdraft, rather than as a measure of parcel origin.

4) CAPE AND CIN

CAPE and CIN were computed for parcels within the RFD by inserting their surface thermodynamic measurements into the inflow sounding nearest to the observed storm in space and time as follows (undiluted ascent from the surface was assumed):

$$\text{CAPE} = -R_d \int_{p_{\text{LFC}}}^{500} (\theta_p - \overline{\theta})\left(\frac{p}{p_o}\right)^{R_d/c_p} d \ln p \quad (10)$$

$$\text{CIN} = -R_d \int_{p_{\text{sfc}}}^{p_{\text{LFC}}} (\overline{\theta} - \theta_p)\left(\frac{p}{p_o}\right)^{R_d/c_p} d \ln p, \quad (11)$$

where p_{LFC} is the pressure of the level of free convection, p_{sfc} is the surface pressure, θ_p is the potential temperature of the lifted parcel, $\overline{\theta}$ is the potential temperature of the environment, and CAPE was only computed below 500 mb, because many of the special soundings launched on operations days were terminated below the equilibrium level. For the soundings containing data to the height of the equilibrium level, on average, approximately 20%–25% of the total CAPE was present below 500 mb.

5) PRESSURE

Pressure was reduced to the average height of the vehicle observations using the integrated hydrostatic equation of the form

[7] The θ_e computed here is really the ''pseudoequivalent potential temperature,'' θ_{ep}, which assumes that liquid water falls out of the parcel, thus its heat-carrying capacity is neglected (Emanuel 1994). Although θ_{ep} is not exactly conserved for moist-adiabatic processes (in which condensed water remains in the parcel), for all practical purposes, it can be considered to be conserved.

$$p = p_{\text{obs}} \exp\left[\frac{(z_{\text{obs}} - \overline{z})g}{R_d \overline{T}_v}\right], \tag{12}$$

where $\overline{z}$ is the average elevation of the mobile mesonet observations within the analysis domain, p is the pressure reduced to $\overline{z}$, p_{obs} is the pressure observed by the mobile mesonet vehicle, z_{obs} is the elevation at which the mobile mesonet pressure p_{obs} was recorded, and $\overline{T}_v$ is approximated as the average virtual temperature (liquid water effects neglected) recorded by the mobile mesonet within the analysis domain.

Elevation data were obtained from U.S. Geological Survey Level 2 Digital Elevation Model (DEM) data. Each 7.5′ unit of DEM coverage has a horizontal resolution of 30 m, a vertical precision of 1 ft (0.31 m), and accuracy equal to or better than one-half of a contour interval of the 7.5′ topographic quadrangle map [corresponds to 2.5–5.0-ft (0.78–1.6 m) accuracy]. Mobile mesonet elevations were obtained from a nearest-neighbor analysis of the DEM data. An analysis of the errors of reduced pressure values, due to DEM errors, GPS position errors, and instrument errors, is presented in the appendix.

d. Specification of the base state

Computations of fluctuations of meteorological variables (e.g., θ_v', θ_e', p') depend on how the base state (e.g., $\overline{\theta}_v$, $\overline{\theta}_e$, $\overline{p}$) is defined. It is difficult to define exactly what constitutes the ''environment'' of a storm; therefore, it also is difficult to define the base state of the atmosphere in the environment of a storm (Brooks et al. 1994b; Markowski et al. 1998).

Although there is more than one way to estimate the base state (and all techniques are arbitrary and imperfect), the base state of a meteorological quantity, $\overline{\xi}$, was estimated by a weighted mean of N convectively uncontaminated surface airways and Oklahoma Mesonet (Brock et al. 1995) observations within a 400-km radius of the updraft, interpolated to the times of tornadogenesis or maximum low-level rotation, where

$$\overline{\xi} = \frac{\sum_{i=1}^{N} w_i \xi_i}{\sum_{i=1}^{N} w_i}, \tag{13}$$

where w_i is the Barnes weight function,

$$w_i = \exp\left(-\frac{r_i^2}{\kappa_o}\right), \tag{14}$$

where r is the distance of the ith uncontaminated observation from the updraft and κ_o is chosen in a manner following Koch et al. (1983), where

$$\kappa_o = 5\left(\frac{2\Delta n}{\pi}\right)^2, \tag{15}$$

where Δn is the average spacing between standard observations [$O(100)$ km]. [The weighted means of convectively uncontaminated observations using $\kappa_1 = 0.5\kappa_o$ and $\kappa_2 = 1.5\kappa_o$ also were computed to examine the sensitivity of the base state to the choice of κ (see appendix).] For cases in which observation density varied considerably across the ''influence region'' (e.g., a case in which a storm was on the Oklahoma border, whereby half of the averaging region contained Oklahoma Mesonet observations at a density of several times the density of surface airways observations), ''superobservations'' were made by combining observations in the observationally dense regions, so that undue weight would not be given to the clustered observations. A base state was not defined for upper-air variables; that is, no attempt was made to construct ''composite'' soundings, from which CAPE and CIN values could be computed. Proximity soundings were used instead, at stated earlier in this section.

Although not rigorously justifiable, precedents do exist for defining the base state in the manner used herein. Fujita (1955, 1963) and Charba and Sasaki (1971) used a technique in which the base state was obtained at each observation location by interpolating from smooth contours obtained from the regular synoptic stations. It may be somewhat unconventional to specify a reference state that is not constant in space of time (because linearization of the primitive equations loses its advantages), but the choice is as arbitrary as the decision to make the reference state a constant with respect to space or time. It is believed that what is important is not so much the exact way the base state is specified, but rather that the base state is *consistently* specified and the *differences* between the cases are examined.

e. Limitations

Limitations are unavoidable in observational research, and those that should be considered in this work are summarized below:

1) Road networks do not allow continuous sampling of moving updrafts for periods longer than about 5 min before repositioning of the vehicle array requires that they temporarily forfeit data collection in critical regions of the storm. Therefore, the time evolution of features is difficult to document. In all but a lucky few cases, all that can be obtained are ''snapshots'' of the hook echo and RFD region at various times from case to case (in some cases, the RFD is sampled near tornadogenesis; at other times, during the mature phase of a tornado; and at other times, during tornado demise). One case by itself probably offers little new knowledge, but the ensemble of snapshots from different times relative to tornadogenesis from a variety of cases hopefully can lead to new understanding.
2) Time-to-space conversion was performed over ~5

min intervals—storms are not steady for 5-min periods, at least not near the time of tornadogenesis (if they were, then tornadogenesis would not occur). In order to maximize the coverage of data gathered by a finite number of vehicles, ~5 min was chosen as the time period over which steadiness was assumed. Past studies have been forced to assume even longer periods of steadiness [e.g., 8–16 min in Johnson et al. (1987)]. Dual-Doppler radar analyses also are not immune from the necessity to assume steadiness for ''short'' periods of time [5–10 min; e.g., Brandes (1977a,b, 1984a,b); Ray (1976); Ray et al. (1981)]. There is some confidence that the choice of $|\Delta t_{\max}|$ of 2–3 min in this work was not too severe; the thermodynamic fields to be presented in section 3 are largely free of noise. If the choice of $|\Delta t_{\max}|$ was made inappropriately large, one might expect that a time-to-space conversion analysis would yield noisy fields, arising from disagreement among observations at similar storm-relative positions at slightly different times. Furthermore, effects other than pure translation (e.g., rotation, differential translation) could be potentially problematic in the time-to-space conversion. These problems cannot be fully addressed without four-dimensional kinematic fields. The results presented in section 3 are crucially dependent on the accuracy of the time-to-space conversion and its associated steady-state assumption.

3) Thermodynamic fields and their gradients cannot be ascertained above the surface by direct means. At best, only the sign of the gradients can be inferred above the surface, based on assumptions of the lapse rates beneath and at a distance from the storm. In future field experiments, we may have a means of obtaining direct observations within RFDs above the ground (e.g., remotely piloted aircraft).
4) It is tempting to only investigate storms at or just prior to the time of tornadogenesis. Caution should be exercised when drawing conclusions based on such analyses—time histories of air parcels (following their trajectories) probably are important, including any baroclinity encountered possibly as much as 30 min or longer prior to tornadogenesis. Although the surface observation density within the RFDs exceeded that in virtually all other previous studies, it still was not possible to compute trajectories over 30-min intervals.

3. Observations

a. RFDs associated with nontornadic supercells

The RFDs associated with nontornadic supercells generally contained relatively large θ_v deficits (typically >5 K) at the surface (Fig. 3).[8] Nontornadic RFDs also were associated with relatively large θ_e deficits (typically >10 K), with midlevel θ_e values commonly being detected at the surface (Fig. 4). Numerous past studies have reported a similar finding (e.g., Browning and Ludlam 1962; Browning and Donaldson 1963; Charba and Sasaki 1971), but the fractions of environmental air and updraft air that compose the RFD cannot be determined from surface θ_e values alone, just as the length of the downward parcel excursions also cannot be ascertained. Surface θ_e values sampled within nontornadic RFDs, on average, were similar to the θ_e values measured at heights (AGL) of 1.5–2.4 km in proximity soundings.

Many RFDs associated with the nontornadic supercells contained surface-based CAPE despite significant surface θ_v and θ_e deficits; however, in most cases, CIN was large within 4 km of the circulations (200–300 J kg^{-1} in 4 of 12 cases, >500 J kg^{-1} in 5 of 12 cases; e.g., Fig. 5). In 3 of 12 cases, at least some surface parcels within 4 km of the circulation center in the RFD did not contain any CAPE, and in 1 of 12 cases, no surface parcels within 2 km of the circulation center contained CAPE. It is important to reiterate that CAPE and CIN values were obtained by inserting RFD surface measurements into *inflow* soundings.

Finally, it is worth noting that in a couple of nontornadic supercell cases, smaller surface θ_v deficits of only 3–5 K were observed in the RFDs, along with more substantial surface-based CAPE (e.g., the Elmwood, Oklahoma, supercell of 8 June 1995). In these cases, however, no CIN values less than 150 J kg^{-1} were detected within a 4-km radius of the circulation centers.

b. RFDs associated with tornadic supercells

The RFDs associated with ''weakly tornadic'' supercells (e.g., those that produced F0–F1 tornadoes that persisted 5 min or less) often had surface thermodynamic characteristics that were similar to the RFDs associated with nontornadic supercells. The surface θ_v and θ_e deficits in these RFDs generally were 4–7 and 10–12 K, respectively, within a few kilometers of the circulation centers (e.g., 2 June 1999; Fig. 6). These surface parcels were associated with generally >100 J kg^{-1} CAPE (below 500 mb) and <150 J kg^{-1} CIN.

In the RFDs associated with much more prolific tornado-producing supercells (e.g., those that produced tornadoes of ≥F2 intensity or tornadoes that persisted >5 min), surface θ_v and θ_e deficits were relatively small (typically <2 and <4 K, respectively, within 2 km of

[8] In this section and the next, only a small, representative subset of the total assembly of surface analyses is included where appropriate. The complete collection of over 200 RFD surface analyses, 30 plots of larger-scale surface observations, and over 30 proximity soundings is available electronically from the corresponding author. This approach was taken in order to keep the length of the paper manageable. Summary statistics are considered in section 3d.

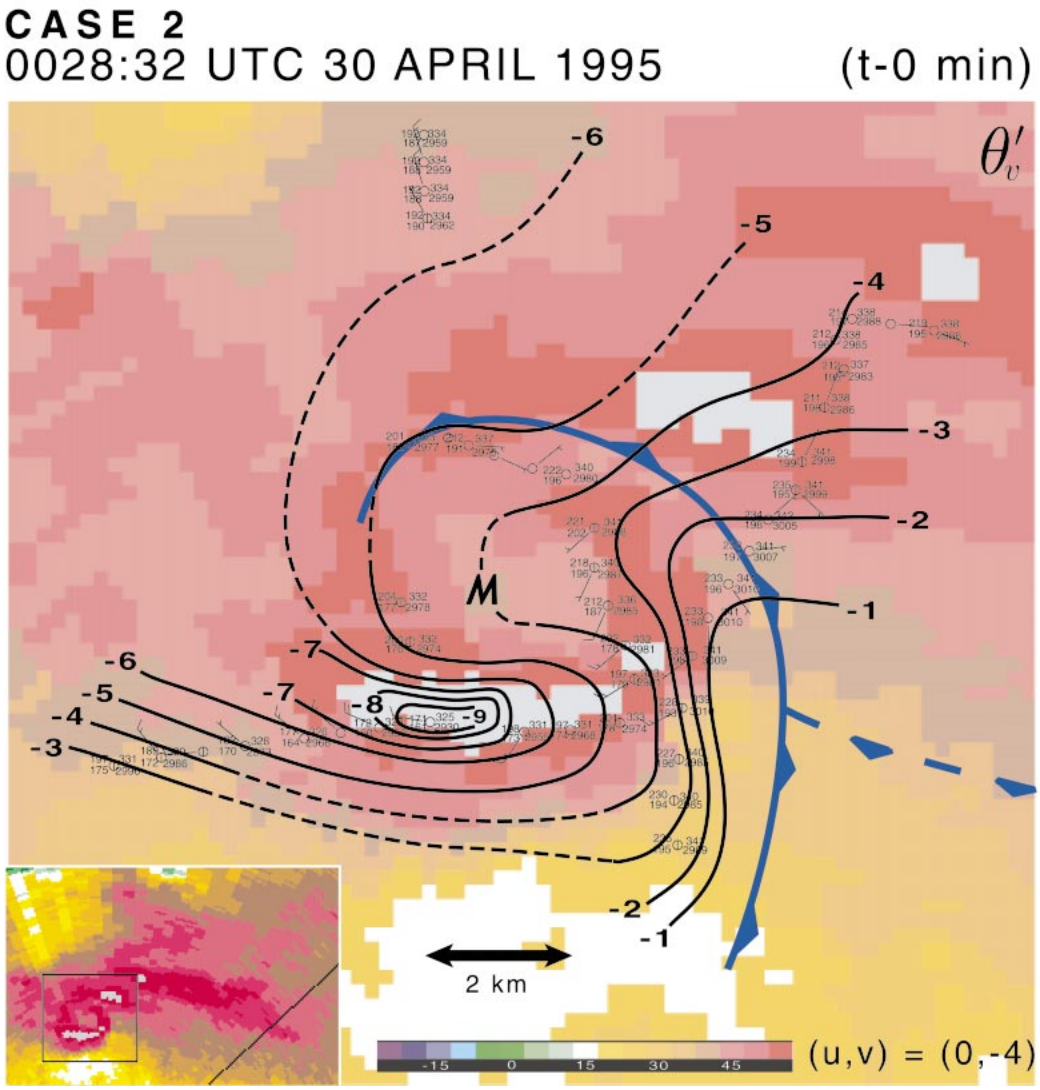

FIG. 3. Subjective analysis of virtual potential temperature fluctuation, θ_v' (K), at 0028:32 UTC 30 Apr 1995. Dashed contours are used in regions where the analysis is less certain owing to low observation density. The ''$t - 0$ min'' indicates that the analysis reference time is 5 min before tornadogenesis failure (the time of strongest low-level rotation on WSR-88D). Mobile mesonet station models include (reading counterclockwise, beginning with the three-digit numeral at the top left) temperature, T, in °C to the nearest 0.1°C with the decimal omitted; dewpoint temperature, T_d, in °C to the nearest 0.1°C with the decimal omitted; virtual potential temperature, θ_v, in K to the nearest 0.1 K with the decimal omitted; and equivalent potential temperature, θ_e, in K to the nearest 1 K. Wind barbs depict storm-relative winds and are in kt (full barb = 10 kt; flag = 50 kt). Mobile mesonet observations have been averaged over 12-s intervals and $|\Delta t_{\max}| = 3$ min was used in the time-to-space conversion. The assumed (u, v) appears near the bottom of the figure. Observations obtained more than 1 min before or after the analysis reference time are ''flagged'' with a vertical bar through the center of the station model. Storm-scale fronts are depicted using conventional frontal symbology (dashed boundaries are drawn where uncertainty exists). The letter M indicates the position of mesocyclone center at the lowest radar elevation angle. Radar reflectivity data were obtained from the NOAA P3 LF radar.

the tornadoes) (e.g., Friona and Dimmitt, Texas, storms of 2 June 1995; Figs. 7 and 8). In a few cases (e.g., cases 18, 19, 20, 24—note that all of these contained a strong tornado), the maximum temperatures and θ_v values observed in the RFD were greater than the inflow values. In such cases, the warm downdrafts *were not simply midlevel environmental air that had descended dry adiabatically* [i.e., the ''heat burst mechanism'': Johnson (1983)]. Instead, these warm downdrafts had small (often <3 K) θ_e deficits, implying that the parcels did *not* have midlevel environmental origins.

The θ_e values measured at the surface within RFDs associated with tornadic supercells generally were similar to values observed at lower altitudes (often <1 km

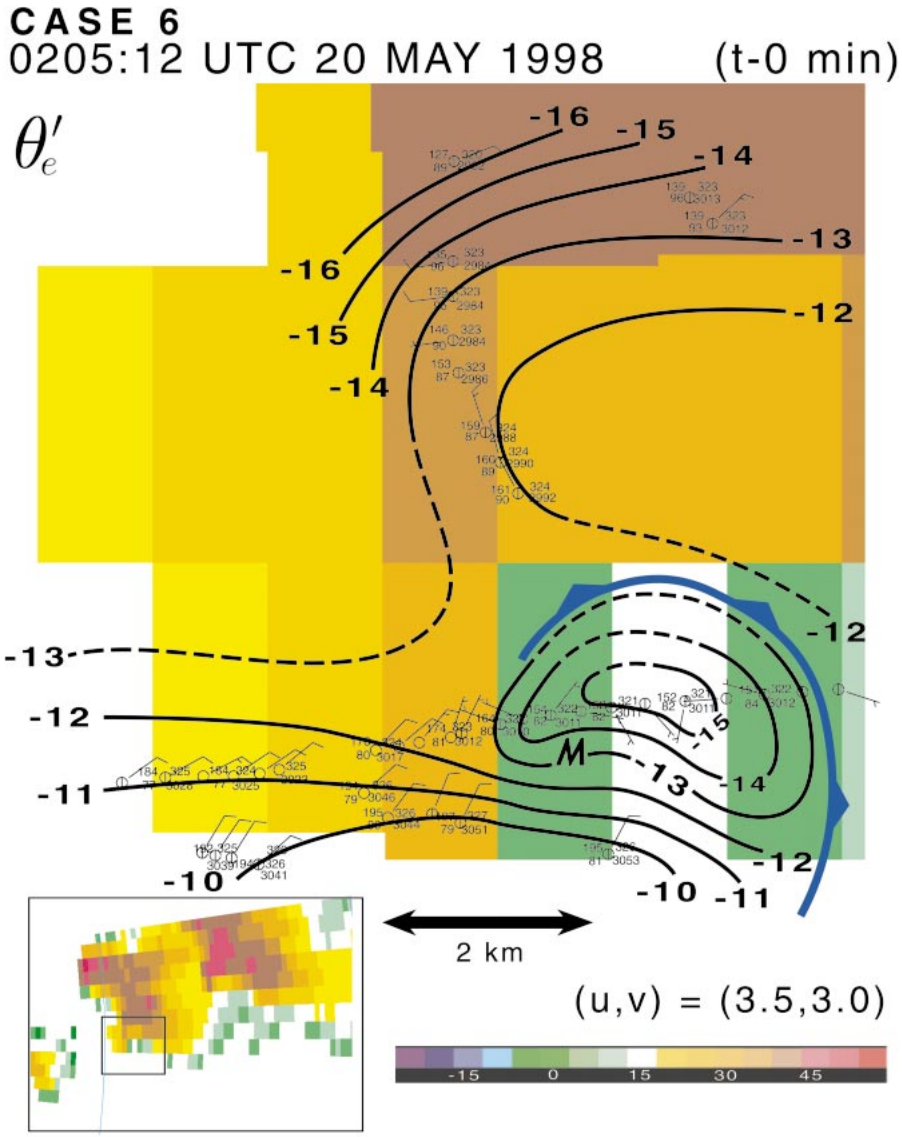

FIG. 4. As in Fig. 3 but θ_e' is analyzed at 0205:12 UTC 20 May 1998. Radar reflectivity data are from the KCYS WSR-88D.

AGL) on nearby soundings, compared to the nontornadic cases. Occasionally RFD θ_e values were similar to inflow θ_e values. Furthermore, all of the RFDs associated with tornadic storms (including F0 and F1 tornado cases) contained surface-based CAPE, with some RFDs containing extreme values of CAPE [e.g., >700 J kg^{-1} below 500 mb on 8 June 1995 and 3 May 1999[9] (Fig. 9)]. Values of CAPE within the RFDs of tornadic supercells increased as tornado intensity and longevity increased, and CIN values within the RFDs were often <50 J kg^{-1}, especially in the portions of the RFD northeast through southeast of the tornadoes.

Although small θ_v and θ_e deficits were detected in most of the RFDs associated with strong tornadoes, in one well-sampled case, a relatively large θ_v and θ_e deficit (up to 7 and 18 K, respectively) was observed within a hook echo associated with a strong (F4), long-lived (>20 min) tornado (case 21: Allison, Texas, 8 June 1995). However, despite the large surface θ_v and θ_e deficits, the relatively cool parcels within the hook echo still were associated with significant surface-based CAPE (>200 J kg^{-1} below 500 mb). It may be noteworthy that large-scale CAPE values for this case were exceptionally large (total CAPE >4000 J kg^{-1}); thus, surface parcels with θ_v values as much as 7 K smaller than those on the large scale still were potentially buoyant. It also may be worth mentioning that warm air

[9] Markowski (2002b) provides a more detailed description of mobile mesonet data on 3 May 1999.

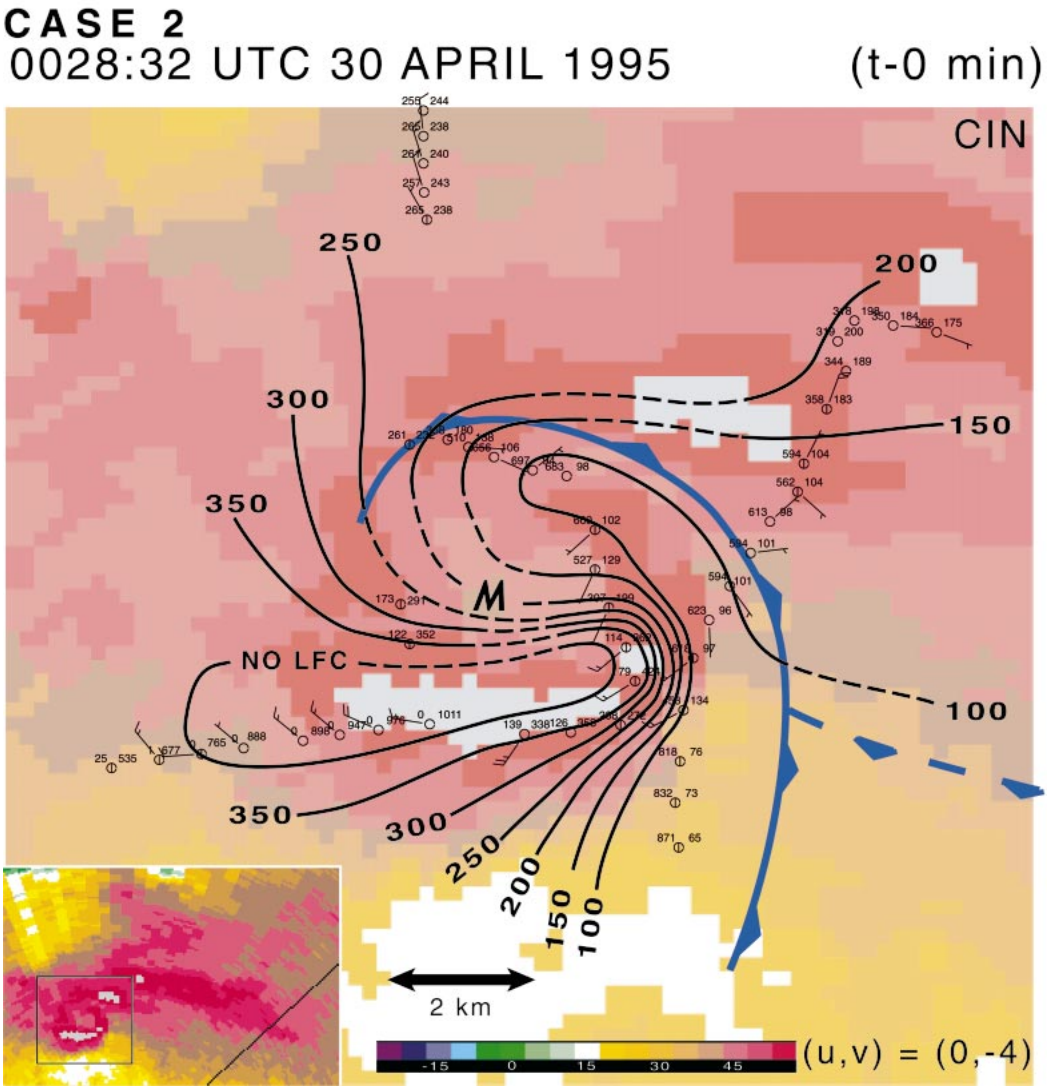

FIG. 5. As in Fig. 3 but CIN is analyzed. Station models display (left) CAPE (below 500 mb) and (right) CIN (J kg^{-1}).

apparently was more widespread within the RFD of this cyclically tornadic supercell during an earlier tornado that it produced near Wheeler, Texas (case 20). Thus, RFD characteristics can vary throughout the lifetime of a supercell.

c. Other observations

In some of the most prolific tornadic storms intercepted (i.e., those that produced more than five tornadoes, some of which were strong or violent; e.g., cases 20, 24, and 25), surface baroclinity within the hook echo and RFD was weak (maximum $|\nabla_h \theta_v'| < 1$ K km^{-1}), absent, or oriented such that horizontal vorticity generation would be antistreamwise (Table 4). These observations argue that surface baroclinity within the hook echo and RFD is not a necessary condition for tornadogenesis. Moreover, the fact that these storms were able to produce so many long-lived, strong tornadoes may imply that the lack of baroclinity was symptomatic of a lack of cold air near the circulation. Relatively cold, stable surface air parcels were found to be more widespread in nontornadic RFDs, as documented in section 3a.

In none of the cases was evidence found of a *separate* ''occlusion downdraft'' in the mobile mesonet data, although it is not clear whether the spatial resolution of the data would allow for the sampling of such a feature, or even exactly how such a feature might manifest itself in surface data. While we agree that the dominant downdraft forcing may be different at various times in the evolution and in various portions of the RFD, the surface data do not appear to indicate that the ''occlusion downdraft'' proposed by Klemp and Rotunno (1983) is more

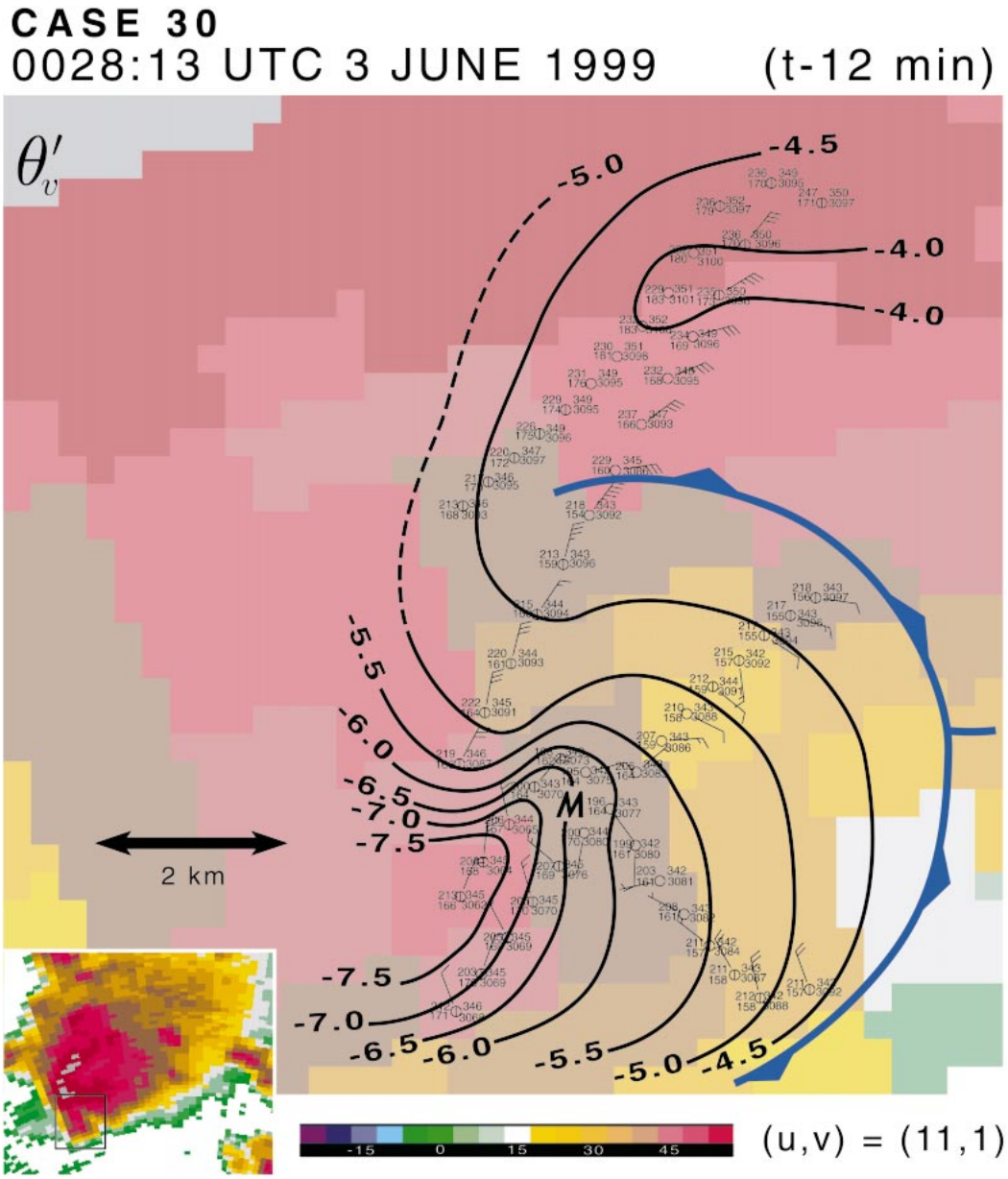

FIG. 6. As in Fig. 3 but at 0028:13 UTC 3 Jun 1999. Radar reflectivity data are from the KLBB WSR-88D radar. The "$t - 12$ min" indicates that the analysis reference time is 12 min before tornadogenesis.

than a surging, intensification of the RFD (e.g., Fig. 3). Furthermore, no evidence was obtained of a tornado occurring prior to or in the absence of the occlusion of the mesocyclone that was originally described by Burgess et al. (1977), Brandes (1978), and Lemon and Doswell (1979).

Relatively high pressure was observed along the RFD gust fronts *and* within the RFDs of both tornadic and nontornadic supercells—both are locations where convergence and divergence are a maximum, respectively, and therefore fluid extension [proportional to $(\partial u/\partial x)^2 + (\partial v/\partial y)^2$] "contributes" to pressure excess there (Rotunno and Klemp 1982) (e.g., Fig. 10). Furthermore, the high pressure regions typically spiraled around the cyclonic vorticity maxima, forming nearly closed annuli of pressure excess, similar to what Fujita (1958) had inferred.

It is worth mentioning that in all but one nontornadic case, a circulation was detected at the surface, in addition to an occluded gust front structure (e.g., Figs. 3 and 4). In fact, the analyses summarized in sections 3a and 3b revealed that the surface gust front structures of the nontornadic and tornadic cases, as resolved by the mobile mesonet, often were indistinguishable, as Wak-

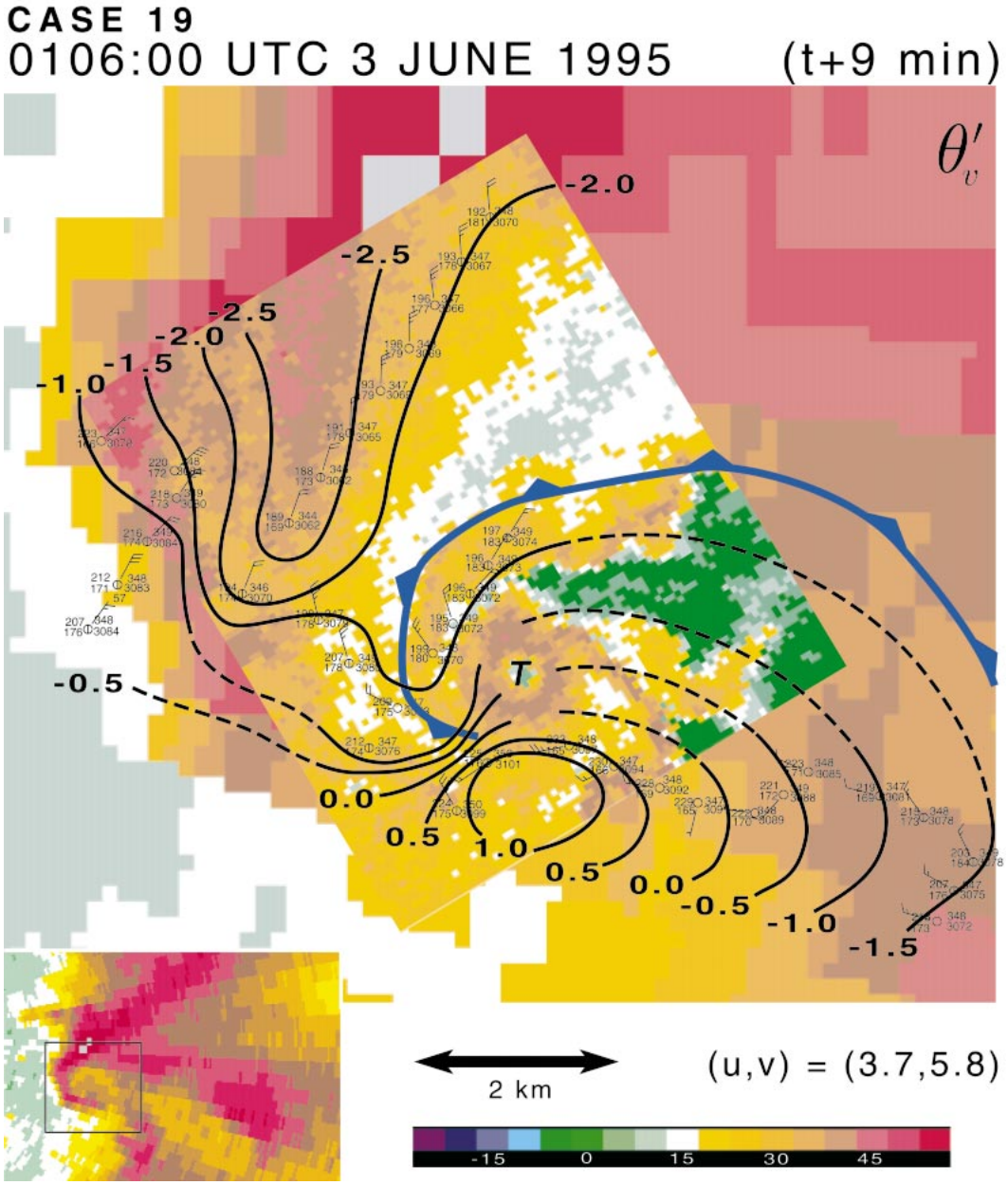

FIG. 7. As in Fig. 6 but at 0106:00 UTC 3 Jun 1995. Radar reflectivity data are from the NOAA P3 LF and DOW (inset) radars. The letter T indicates the tornado position.

imoto and Cai (2000) also found in their comparison of the Garden City, Kansas (tornadic), and Hays, Kansas (nontornadic), supercells during VORTEX. The only apparent significant difference appears to be the low-level stability. Furthermore, in a couple of cases, tornadogenesis occurred many minutes (as many as 10–15 min) after the occlusion of the low-level mesocyclone (e.g., Fig. 6).

Three-dimensional cloud simulation studies using a Kessler microphysics parameterization (Kessler 1969) have found the ''undercutting'' of the circulation by outflow to be detrimental to storm sustenance (and presumably tornadogenesis) (Wilhelmson and Klemp 1978; Weisman and Klemp 1982; Brooks et al. 1993, 1994a,b; Gilmore and Wicker 1998). However, in only one observed case did a circulation appear to be undercut by outflow (and consequently, no surface circulation was detected). This tornadogenesis failure mechanism may not be as common as suggested by previous simulation studies. However, it is possible that many storms that were undercut by RFD outflow were not sampled; updrafts that visually appeared to be undercut often were

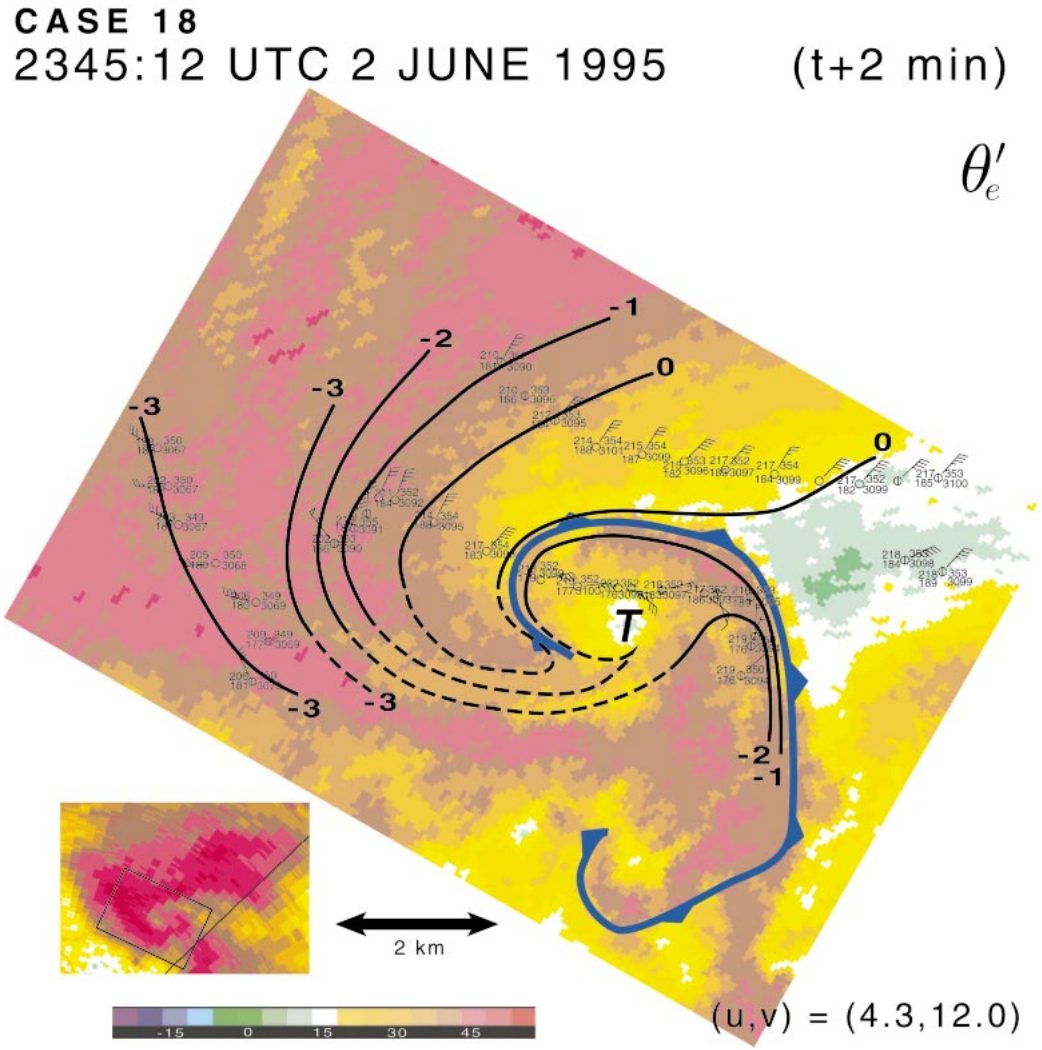

FIG. 8. As in Fig. 6 but θ'_e is analyzed at 2345:12 UTC 2 Jun 1995. Radar reflectivity data are from the DOW radar and NOAA P3 LF radar (lower left).

abandoned during field operations in favor of storms that did not appear visually to be undercut.

Finally, several previous studies have analyzed a couplet of vertical vorticity straddling the hook echo and RFD (e.g., Ray et al. 1975, 1981; Brandes 1977b, 1978, 1981, 1984a; Fujita and Wakimoto 1982), although the feature understandably has escaped recognition in many of the past studies. The mobile mesonet detected a similar couplet of vertical vorticity at the surface within both tornadic and nontornadic RFDs, when sampling allowed (e.g., Figs. 4 and 7). These couplets probably are indications that RFDs are involved in a downward tilting of vortex lines, perhaps necessarily supplying circulation to the tornado, as many others previously have hypothesized (e.g., Ludlam 1963; Fujita 1975; Burgess et al. 1977; Barnes 1978a; Lemon and Doswell 1979). No differences between the appearance of the couplet in the tornadic and nontornadic cases was observed at the surface.

d. Comparison of nontornadic and tornadic RFDs

RFD characteristics for each case and mean RFD characteristics are summarized in Tables 4 and 5, respectively. A 4-km radius from the circulation center was used for the minimum θ'_v, θ'_e, and CAPE values, and for the maximum z_o and CIN values that appear in the tables; however, a 2-km radius was used for the maximum θ'_v, θ'_e, and CAPE, and for the minimum z_o and CIN values that appear in the tables. The arbitrary choice of using a smaller radius for the latter variables was made because we felt that warm regions in the wake of the updraft, in regions where streamlines clearly diverge from the circulation and do not enter it, should

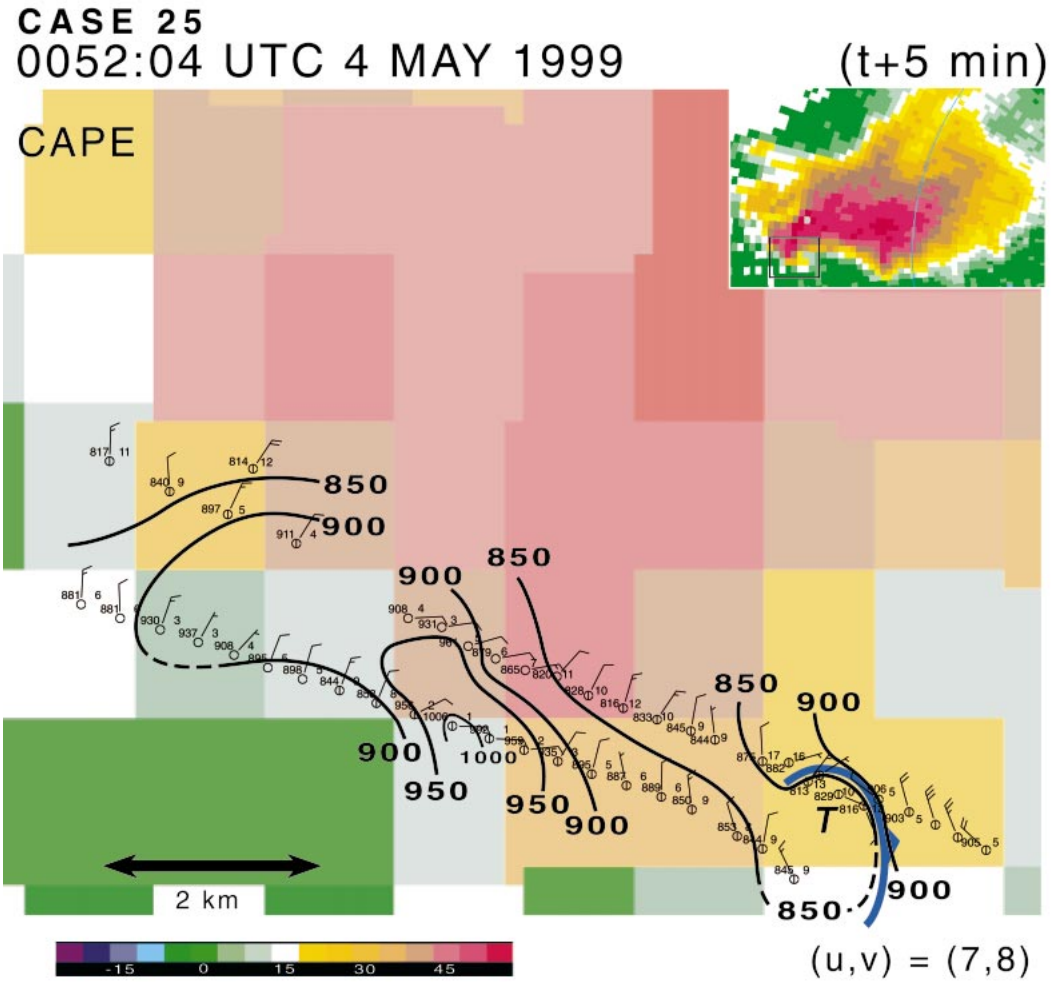

FIG. 9. As in Fig. 6 but CAPE is analyzed at 0052:04 UTC 4 May 1999. Radar reflectivity data are from the KTLX WSR-88D. Station models display CAPE and CIN as in Fig. 5

not be considered in the results. In Figs. 11 and 12, the results are summarized graphically by way of scatterplots.

In Table 5 and in Figs. 11 and 12, the differences in the means of the groups were compared to determine if they were statistically significant. The common test for significance is the *t* test; however, a different approach was used instead, following Mielke et al. (1981). The same approach was used by Blanchard and Lopez (1985) and Rasmussen and Blanchard (1998), and is well summarized by Blanchard and Lopez (1985): ''The (*t*-test) . . . assumes that the data sample follows the normal distribution. Since many atmospheric parameters are not normally distributed, but rather are highly skewed, this standard parametric test is inappropriate. A nonparametric test called Multi-Response Permutation Procedures (MRPP) is well suited to (atmospheric) data because it makes no assumption about the distribution of the population (Mielke et al. 1976, 1981). MRPP examines and compares the different data groups to determine whether they are from the same or different populations and gives the result in the form of a *P*-value of statistical significance.'' MRPP can be used to indicate the similarity of any number of populations (two in this case: tornadic and nontornadic), and can be performed on one or several variables. The *P* value is the probability that two sets of observations come from the same population (or $1 - P$ is the probability that two populations are different).

The RFDs associated with tornadic supercells were approximately 3–4 K (3–5 K) warmer than the RFDs associated with nontornadic supercells, in terms of θ_v' (θ_e'), on average (Table 5; also see Figs. 11 and 12). Moreover, parcels reaching the surface in nontornadic RFDs had θ_e values similar to the θ_e values observed on soundings at elevations approximately 1 km AGL higher than in tornadic RFDs (Table 5). Surface-based CAPE (below 500 mb) was approximately 300 J kg^{-1} larger in the RFDs associated with tornadic supercells than in those associated with nontornadic supercells, on

average (Table 5). CIN was approximately 150–200 J kg^{-1} larger in the RFDs of nontornadic supercells compared to tornadic supercells, on average (Table 5).

No significant differences were detected between the surface baroclinity ($\nabla_h \theta_v'$) within the hook echoes of nontornadic and tornadic supercells (Table 5). Furthermore, the pressure fields within RFDs associated with nontornadic supercells were not significantly different from those associated with tornadic supercells (Table 5). Perhaps the magnitude of p' is related largely to the strength of the downdrafts (i.e., perhaps p' is due largely to dynamic effects), which does not appear to be related to tornadogenesis based on the lack of observations of obvious differences between the RFD surface divergence in the nontornadic and tornadic cases. (Using a Bernoulli equation, it is easy to show that stronger downdrafts must contain larger p' in order to deflect streamlines at the surface toward the horizontal.)

Whereas the above comparisons represent the average differences, mean θ_v', θ_e', CAPE, and CIN values were computed *by quadrant* (refer to Fig. 2) for nontornadic, ''weakly tornadic'' (defined arbitrarily as producing F0–F1 tornadoes for $\leq$5 min), and ''significantly tornadic'' (those producing long-lived F0–F1 tornadoes or $\geq$F2 tornadoes) supercells (Fig. 13). The largest surface thermodynamic differences between RFDs associated with tornadic and nontornadic supercells were detected east of the circulation centers (quadrants I and IV). In terms of θ_v' and θ_e', RFDs associated with weakly tornadic supercells were more similar to those associated with nontornadic supercells than those associated with significantly tornadic supercells. On the other hand, in terms of CAPE and CIN, in quadrants II and III, RFDs associated with weakly tornadic and significantly tornadic supercells both differed from nontornadic RFDs by approximately similar amounts. Finally, the most significant observational findings also are highlighted by way of a composite illustration that generalizes the main characteristics of RFDs associated with nontornadic and tornadic supercells (Fig. 14).

e. RFD forcing mechanisms

It is possible that the relatively small θ_e deficits observed at the surface in the RFDs associated with tornadic supercells simply indicate that the RFD parcel excursions in tornadic RFDs are shorter than those in nontornadic RFDs. It is equally plausible that the observations of small θ_e deficits within tornadic RFDs imply that the entrainment of midlevel, potentially cold (low θ_e) air, and subsequent evaporation of updraft hydrometeors, play a smaller role in driving the RFDs than in nontornadic supercells. If downward parcel excursions are large (i.e., if RFD parcels arriving at the surface originate from a level where environmental θ_e is much smaller than at the surface), the only means by which downdraft air parcels can reach the surface with θ_e values within a few degrees kelvin of the inflow values is if air parcels *within the updraft* (which contains θ_e values similar to the low-level inflow) are forced to descend owing to precipitation drag or downward-directed nonhydrostatic pressure gradients. Below cloud base, evaporation of precipitation within the RFD and hook echo can occur, and this process essentially conserves θ_e but reduces θ_v. Surface θ_v deficits within RFDs associated with tornadic supercells also were generally small ($<$3 K), implying that large amounts of evaporative cooling generally did not occur in the subcloud layer within the hook echoes associated with tornadic supercells.

Within the RFDs associated with nontornadic supercells, the finding of generally large ($>$8 K) surface θ_e deficits suggests that entrainment of midlevel environmental air (characterized by low θ_e typically) plays a significant role in driving nontornadic RFDs, as in longstanding conceptual models (e.g., Browning and Ludlam 1962; Browning and Donaldson 1963). Hail melting also may play a significant role in the generation of the relatively large θ_e deficits. It cannot be known whether mainly *updraft air* initially undergoes forced descent (owing to precipitation drag or dynamic pressure gradients in a manner similar to that which was hypothesized to occur in tornadic supercells) during which mixing dilutes the θ_e of the descending parcels, or whether the descent in nontornadic RFDs is initiated by the impingement of midlevel *environmental* air, which subsequently becomes negatively buoyant owing to the evaporation and melting of condensate. We also cannot refute the possibility that all RFDs are cold aloft, while some (e.g., those associated with tornadic supercells) warm compressionally near the ground following a loss of condensate to evaporation.

f. Reconciliation of findings with past observations

Observations were made on several occasions from the 1950s through the 1970s of low θ_e and θ_w air at the surface within RFDs (e.g., van Tassell 1955; Beebe 1959; Ward 1961; Browning and Ludlam 1962; Browning and Donaldson 1963; Charba and Sasaki 1971; Lemon 1976; Nelson 1977; Brandes 1977a; Barnes 1978a,b). A major finding of this research, as presented in sections 3a and 3b, is that cold temperatures and low θ_e/θ_w RFD air are associated with tornadogenesis *failure*. In this section we attempt to reconcile this finding with past observations of cold temperatures and *low* θ_e/θ_w RFD air.

Many of the observations of significant T and θ_e deficits in the literature were observed in nontornadic, rather than tornadic, supercells. Among these include Browning and Ludlam's (1962) study of the Wokingham, England, supercell; Lemon's (1976) analysis of a supercell on 25 June 1969; Brandes's (1977a) analysis of a supercell on 6 June 1974; and Nelson's (1977) analysis of a supercell on 25 May 1974.

The eyewitness reports of ''cold'' downdrafts docu-

TABLE 4. Summary of RFD observations. The horizontal line toward the middle of the table separates the nontornadic cases from the tornadic cases. Analysis times are in UTC, with the minutes before (<0) or after (>0) tornadogenesis or tornadogenesis failure provided in parentheses. Values of θ_v' and θ_e' are in K, values of z_o are in km, values of CAPE and CIN are in J kg^{-1}, values of the maximum horizontal θ_v' gradient ($\nabla_h\theta_v'$) are in K km^{-1}, and values of p' are in mb. The uncertainty (see the appendix) appears beside each θ_v', θ_e', z_o, CAPE, CIN, and p' value, along with the quadrant(s) where the measurement was obtained (e.g., I, II, III, or IV, as defined in section 2). The words ''within 4 km'' and ''within 2 km'' refer to the region within a 4-km and 2-radius *within the RFD,* respectively, of the tornado or mesocyclone center. CAPE has only been integrated up to 500 mb, as discussed in section 2. Values of the maximum $\nabla_h\theta_v'$ only are considered if the baroclinic generation has a streamwise component (i.e., only if the sense of the horizontal baroclinic vorticity generated is such that tilting yields cyclonic vertical vorticity). For example, if the only baroclinity detected for a case is oriented such that horizontal vorticity generation has an antistreamwise component, then the value entered in the table for the maximum $\nabla_h\theta_v'$ is zero. In some cases, z_o could not be determined because θ_e values measured at the surface were all larger than those observed on the proximity sounding.

Case	Analysis time	Min θ_v' within 4 km	Max θ_v' within 2 km	Min θ_e' within 4 km	Max θ_e' within 2 km	Min z_o within 2 km
1	2248:00 (−4)	−6.4 ± 0.4 (II)	−4.1 ± 0.4 (III)	−21.1 ± 2.9 (II)	−3.1 ± 2.9 (III)	0.1 ± 0.2 (III)
2	0028:32 (0)	−9.3 ± 0.6 (III)	−3.6 ± 0.6 (I)	−18.1 ± 2.7 (III)	−3.1 ± 2.7 (I)	0.2 ± 0.2 (I)
3	2311:39 (0)	−6.3 ± 0.5 (III)	−3.8 ± 0.7 (IV)	−9.6 ± 2.6 (III)	−9.4 ± 2.6 (I)	1.9 ± 0.5 (IV)
4	0013:20 (0)	−5.2 ± 0.7 (III)	−1.2 ± 0.7 (IV)	−11.7 ± 2.7 (III)	−3.7 ± 2.7 (IV)	2.0 ± 0.3 (IV)
5	2014:43 (0)	−5.6 ± 0.5 (II)	−3.5 ± 0.8 (I)	−12.1 ± 2.6 (II)	−8.0 ± 2.6 (IV)	1.0 ± 0.8 (IV)
6	0205:12 (0)	−11.1 ± 0.5 (II)	−4.2 ± 0.5 (IV)	−13.5 ± 2.5 (II)	−9.5 ± 2.5 (IV)	2.6 ± 0.1 (IV)
7	0133:43 (−12)	−9.7 ± 0.9 (II)	−5.7 ± 0.9 (I)	−6.7 ± 2.5 (III)	−2.7 ± 2.5 (I)	0.2 ± 0.1 (I)
8	0116:06 (−10)	−6.2 ± 0.7 (III)	−4.0 ± 0.7 (IV)	−21.7 ± 2.6 (II)	−14.7 ± 2.6 (IV)	1.2 ± 0.1 (IV)
9	0211:06 (0)	−6.2 ± 0.7 (II)	−3.0 ± 0.8 (IV)	−16.0 ± 2.5 (II)	−8.1 ± 2.6 (IV)	2.4 ± 0.2 (IV)
10	2137:00 (3)	−11.8 ± 0.6 (I)	−6.7 ± 0.6 (IV)	−12.9 ± 2.8 (I)	−6.9 ± 2.8 (IV)	1.7 ± 0.2 (IV)
11	2151:08 (0)	−8.9 ± 0.4 (III)	−4.9 ± 0.4 (III)	−4.0 ± 2.5 (IV)	+5.0 ± 2.5 (IV)	Unknown
12	0101:00 (5)	−4.3 ± 0.x (II)	−2.7 ± 0.x (IV)	−3.1 ± 2.x (II)	−2.3 ± 2.x (IV)	Unknown
13	2349:30 (−14)	−8.4 ± 0.5 (II)	−5.8 ± 0.5 (II)	−16.4 ± 2.5 (I)	−9.4 ± 2.5 (III)	1.3 ± 0.3 (III)
14	2221:06 (−7)	−10.8 ± 0.5 (III)	−7.1 ± 0.4 (III)	−8.9 ± 2.6 (III)	−2.1 ± 2.5 (III)	0.8 ± 0.3 (III)
15	2255:55 (0)	−5.5 ± 0.5 (II)	+0.1 ± 0.5 (IV)	−18.4 ± 2.5 (II)	−1.4 ± 2.5 (IV)	0.2 ± 0.2 (IV)
16	0048:32 (−1)	−4.3 ± 0.5 (IV)	−2.7 ± 0.5 (III)	−16.1 ± 2.6 (III)	−10.1 ± 2.6 (IV)	1.0 ± 0.1 (IV)
17	0138:00 (0)	−2.4 ± 0.5 (II)	−0.6 ± 0.5 (III)	−11.8 ± 2.6 (III)	−0.8 ± 2.6 (I)	0.4 ± 0.2 (I)
18	2345:12 (2)	−2.7 ± 1.0 (III)	−0.1 ± 0.7 (II)	−3.7 ± 2.7 (III)	−1.2 ± 2.7 (II)	1.0 ± 0.1 (II)
19	0106:00 (9)	−3.0 ± 0.8 (II)	+1.0 ± 0.8 (III)	−8.0 ± 2.6 (II)	−2.0 ± 2.6 (III)	0.3 ± 0.1 (III)
20	0022:00 (47)	−2.4 ± 0.6 (III)	−0.3 ± 0.5 (I)	−7.1 ± 3.2 (II)	−1.1 ± 2.7 (III)	Unknown
21	0101:00 (16)	−7.2 ± 0.5 (III)	+0.3 ± 1.0 (II)	−19.2 ± 2.7 (III)	−2.2 ± 2.9 (II)	Unknown
22	0146:22 (11)	−2.1 ± 0.4 (III)	−1.3 ± 0.4 (IV)	−6.8 ± 2.5 (III)	−4.8 ± 2.5 (IV)	0.2 ± 0.1 (IV)
23	0042:00 (0)	−2.9 ± 0.7 (III)	−1.0 ± 0.7 (IV)	−2.0 ± 2.6 (III)	0.0 ± 2.6 (IV)	0.2 ± 0.9 (IV)
24	2219:08 (−1)	−1.3 ± 0.5 (I)	−0.1 ± 0.5 (IV)	−3.2 ± 2.5 (IV)	−1.2 ± 2.5 (IV)	Unknown
25	0052:04 (5)	−0.5 ± 0.5 (II)	+0.1 ± 0.5 (I)	−2.0 ± 2.5 (II)	−1.0 ± 2.5 (I)	Unknown
26	2311:16 (−2)	−5.7 ± 0.7 (IV)	−3.5 ± 0.7 (I)	−5.0 ± 2.5 (IV)	−3.0 ± 2.5 (III)	Unknown
27	2125:00 (0)	−6.6 ± 0.7 (II)	−2.0 ± 1.7 (III)	−4.1 ± 3.2 (II)	0.0 ± 3.2 (III)	Unknown
28	0036:44 (8)	−10.4 ± 0.5 (II)	−5.0 ± 0.5 (I)	−18.6 ± 2.6 (III)	−5.6 ± 2.6 (II)	0.1 ± 0.1 (II)
29	0007:27 (1)	−4.5 ± 0.5 (II)	−0.8 ± 0.5 (III)	−10.1 ± 3.0 (II)	−5.1 ± 3.0 (III)	Unknown
30	0028:13 (−12)	−7.9 ± 0.4 (III)	−4.6 ± 0.4 (I)	−12.2 ± 2.7 (I)	−8.2 ± 2.7 (II)	0.4 ± 0.1 (II)

mented by van Tassell (1955) and Beebe (1959) near the Scottsbluff, Nebraska, tornado may be the most difficult observations to reconcile. The observations were reportedly within 1 km of the tornado, to its south. However, we cannot know precisely how cold (in terms of T and θ_e/θ_w) the downdrafts were because no meteorological instrumentation was present, nor do we know exactly what time the observations were made relative to the occurrence of the tornado. Ward's (1961) observations of ''cold'' air also were made without a thermometer, and the observations were a ''couple miles'' southwest of the tornado.

Other observations of low θ_e air in RFDs associated with tornadic storms were documented on 3 April 1964 by Charba and Sasaki (1971), in the Geary, Oklahoma, supercell analyzed by Browning and Donaldson (1963), and in two tornadic supercells on 29 April 1970 that Barnes (1978a,b) studied. In all of these examples, however, the surface data were of much lower horizontal resolution than the resolution afforded by the mobile mesonet. For example, in Charba and Sasaki's study, surface observing stations (in a mesonetwork) were spaced 20–30 km apart, and in Barnes' studies, the observing stations were spaced 8–9 km apart. The regions of relatively small θ_e and θ_v deficits documented in the tornadic RFDs in this paper were characterized by a horizontal length scale of only a few kilometers; a network of stations spaced 10 km apart would not sample the possibly critical, near-tornado RFD air mass unless by luck. Therefore it is believed that the resolution of the observing systems available in past studies simply did not allow for the detection of relatively warm RFDs in tornadic supercells on a consistent basis.

It may be worth adding that Klemp et al. (1981) found low θ_e air in their simulation of the 20 May 1977 Del City, Oklahoma, tornadic supercell. While their simulation appeared to have many similarities with the observed Del City storm, no direct measurements of low

TABLE 4. (*Extended*)

Max z_o within 4 km	Min CAPE within 4 km	Max CAPE within 2 km	Min CIN within 4 km	Max CIN within 2 km	Max $\nabla_h\theta_v'$ within RFD	Max p' within RFD
1.5 ± 0.2 (II)	202 ± 72 (II)	830 ± 203 (III)	20 ± 29 (III)	405 ± 168 (II)	2.8 (II)	1.4 ± 0.8 (III)
2.8 ± 0.3 (III)	0 ± 0 (III)	669 ± 145 (I)	102 ± 25 (I)	1011 ± 187 (III)	6.1 (III)	0.9 ± 0.8 (III)
2.0 ± 0.5 (III)	57 ± 49 (IV)	116 ± 54 (III)	454 ± 53 (III)	533 ± 64 (IV)	Unknown	0.7 ± 1.2 (III)
2.5 ± 0.2 (III)	93 ± 42 (III)	386 ± 98 (IV)	31 ± 18 (IV)	445 ± 85 (III)	3.9 (III)	0.1 ± 0.8 (III)
1.4 ± 0.8 (II)	355 ± 67 (II)	477 ± 92 (III)	119 ± 26 (III)	205 ± 66 (II)	0.7 (II)	1.0 ± 0.7 (III)
5.4 ± 0.6 (II)	0 ± 0 (I,II)	23 ± 24 (III)	437 ± 71 (III)	901 ± 137 (I)	1.5 (II)	3.6 ± 0.7 (I)
0.4 ± 0.1 (III)	111 ± 89 (II)	177 ± 56 (I)	199 ± 49 (II)	271 ± 61 (II)	1.0 (II)	4.4 ± 0.8 (III)
1.7 ± 0.1 (II)	75 ± 55 (II)	196 ± 63 (IV)	439 ± 66 (IV)	609 ± 79 (II)	1.1 (III)	6.9 ± 0.8 (III)
3.1 ± 0.2 (II)	0 ± 0 (I-IV)	0 ± 0 (I–IV)	983 ± 137 (IV)	1041 ± 175 (III)	3.0 (I)	3.1 ± 0.8 (III)
1.9 ± 0.2 (I)	127 ± 49 (I)	337 ± 52 (IV)	246 ± 71 (IV)	559 ± 82 (I)	3.1 (III)	1.4 ± 0.8 (II)
1.2 ± 1.2 (IV)	98 ± 35 (III)	333 ± 126 (I)	5 ± 28 (I)	252 ± 94 (III)	0.9 (II)	2.2 ± 0.6 (III)
Unknown	96 ± 34 (III)	379 ± 165 (IV)	8 ± 10 (IV)	289 ± 97 (III)	0.5 (III)	2.4 ± 0.6 (III)
1.9 ± 0.3 (I)	93 ± 47 (I)	238 ± 108 (III)	208 ± 96 (III)	391 ± 112 (I)	2.8 (II)	0.3 ± 0.8 (II)
2.1 ± 0.3 (III)	100 ± 46 (III)	299 ± 71 (III)	363 ± 77 (III)	610 ± 142 (III)	Unknown	0.6 ± 0.8 (II)
1.6 ± 0.2 (II)	0 ± 0 (II,III)	302 ± 86 (IV)	50 ± 47 (IV)	842 ± 145 (III)	3.9 (II)	1.3 ± 0.8 (III)
1.3 ± 0.1 (III)	112 ± 50 (III)	433 ± 71 (IV)	284 ± 53 (IV)	646 ± 79 (III)	Unknown	2.1 ± 0.7 (IV)
1.5 ± 0.1 (III)	268 ± 62 (III)	620 ± 84 (I)	171 ± 48 (I)	438 ± 64 (III)	1.3 (II)	1.4 ± 0.7 (II)
1.4 ± 0.1 (III)	345 ± 93 (IV)	511 ± 89 (II)	6 ± 12 (II)	57 ± 26 (IV)	1.5 (III)	7.0 ± 0.8 (IV)
1.2 ± 0.2 (II)	147 ± 48 (I)	383 ± 81 (III)	31 ± 30 (III)	270 ± 65 (II)	1.1 (II)	1.4 ± 0.7 (IV)
1.4 ± 0.1 (II)	571 ± 78 (II)	707 ± 101 (III)	19 ± 24 (III)	59 ± 40 (II)	0.8 (II)	−0.5 ± 0.8 OI)
1.8 ± 0.1 (III)	159 ± 62 (III)	673 ± 125 (II)	26 ± 32 (II)	481 ± 45 (III)	6.0 (III)	2.9 ± 0.9 (IV)
0.4 ± 0.1 (III)	199 ± 83 (IV)	273 ± 100 (IV)	209 ± 43 (IV)	242 ± 56 (IV)	Unknown	−0.6 ± 0.7 (IV)
0.8 ± 0.9 (III)	159 ± 80 (III)	345 ± 103 (IV)	15 ± 9 (IV)	77 ± 38 (*V)	1.9 (III)	2.8 ± 0.7 (III)
Unknown	821 ± 131 (IV)	986 ± 106 (III)	2 ± 14 (III,IV)	11 ± 12 (IV)	0.0	0.4 ± 0.8 (III,IV)
Unknown	793 ± 126 (II)	947 ± 116 (II)	2 ± 12 (II)	17 ± 13 (II)	0.6 (II)	0.6 ± 0.8 (III)
Unknown	334 ± 63 (I)	519 ± 87 (III)	18 ± 21 (III)	79 ± 37 (IV)	1.3 (III)	1.3 ± 0.8 (II)
Unknown	364 ± 69 (III)	577 ± 76 (III)	190 ± 25 (III)	265 ± 74 (II)	0.3 (II)	2.2 ± 0.6 (III)
1.1 ± 0.1 (III)	0 ± 0 (III)	250 ± 63 (II)	561 ± 86 (II)	1314 ± 180 (III)	4.2 (II)	1.1 ± 0.7 (III)
Unknown	566 ± 83 (II)	996 ± 208 (III)	3 ± 18 (III)	119 ± 57 (II)	5.7 (II)	0.0 ± 0.8 (II)
0.8 ± 0.2 (I)	38 ± 49 (IV)	233 ± 88 (III)	390 ± 101 (III)	570 ± 184 (IV)	2.5 (II)	2.6 ± 0.7 (II)

θ_e air in the RFD within a few kilometers of the tornado were made. Brandes (1981) did hypothesize, however, from his analysis of the Del City storm, that the RFD was thermodynamically driven. But this conclusion was based on the apparent erosion of midlevel echo, and not on direct observations of low θ_e air at the surface.

4. Anticipation of surface RFD characteristics from environmental data

The findings presented in the previous section, while perhaps significant, cannot directly benefit operational meteorologists responsible for issuing tornado warnings unless some means can be found for inferring ''unobservable scale'' RFD characteristics from routinely collected ''observable scale'' data. In this section we briefly summarize the results of comparisons between RFD characteristics and data obtained from soundings and regularly available surface observations.

As stated earlier, the finding of surface θ_v and θ_e differences between the RFDs of nontornadic and tornadic supercells may suggest that the entrainment of midlevel environmental air is less significant in tornadic supercells. Sounding and hodograph parameters that were believed to be potentially relevant for the production of θ_v and θ_e deficits within RFDs were compared to RFD characteristics for each case. These characteristics included midlevel dewpoint depression (T_{dd}), storm-relative winds, and vertical wind shear magnitudes. Furthermore, surface dewpoint depressions ($T_{dd_{\rm sfc}}$) were analyzed in the inflow of all of the storms for it was believed that this quantity may be a measure of the potential for cooling due to subcloud-layer evaporation of hook echo precipitation within the RFD (the values recorded represented an average of the minimum and maximum T_{dd} values observed within a sector of arc width 90°, centered on the storm motion vector).

The most representative sounding was sought for each

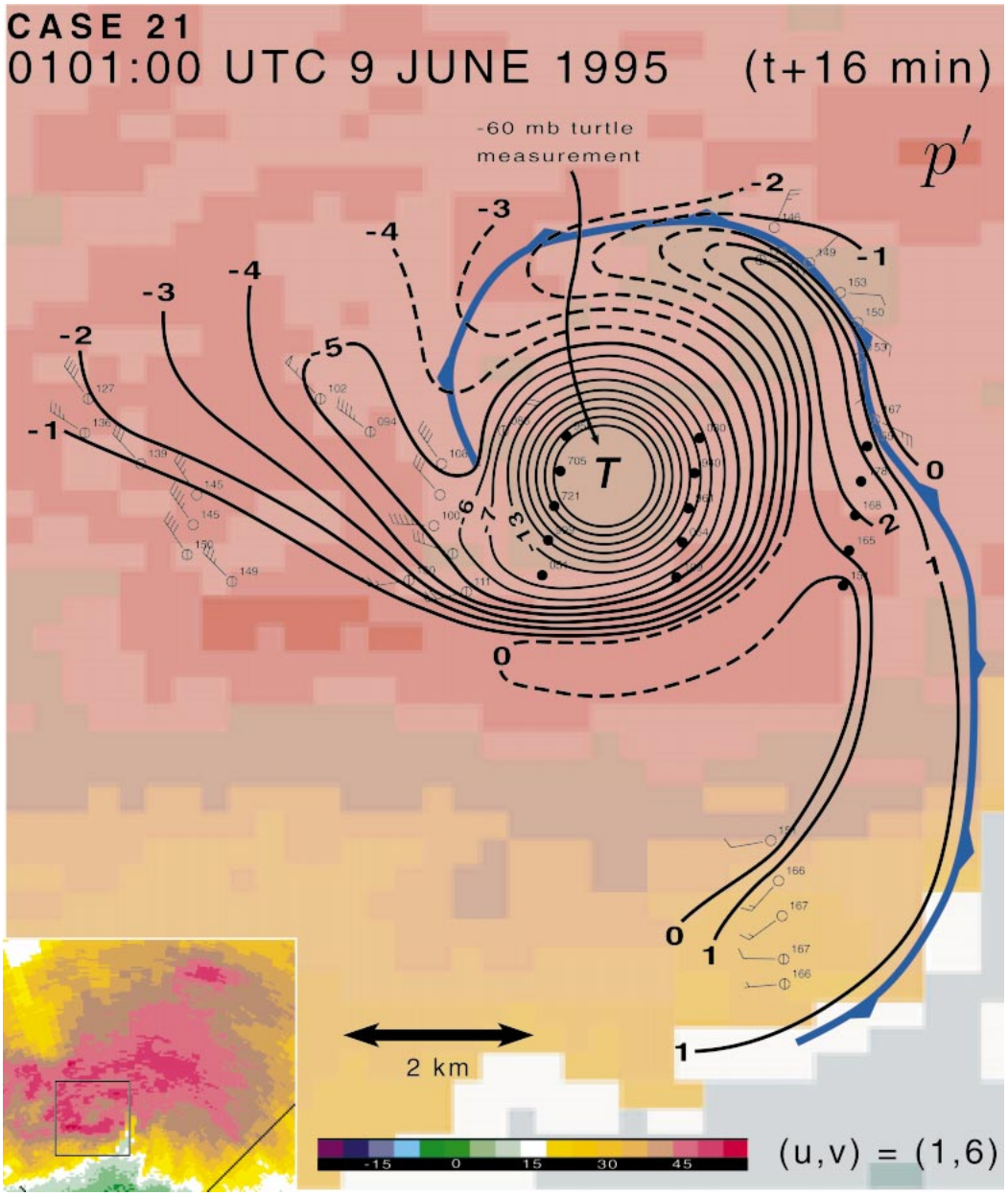

FIG. 10. As in Fig. 6 but p' is analyzed at 0101:00 UTC 9 Jun 1995. Filled circles indicate observations from turtles deployed by New Mexico Institute of Mining and Technology (Winn et al. 1999). Pressures to the nearest 0.1 mb appear in the station models with the leading 9 omitted in most of the observations. A few of the turtle measurements have the leading 8 omitted. The contour interval is 1 mb except for $p' < -7$ mb, for which the interval is 6 mb. Radar reflectivity data are from the NOAA P3 LF radar.

of the 30 cases; however, the definition of storm ''environment'' is ambiguous. Darkow (1969), Darkow and McCann (1977), and Kerr and Darkow (1996) used the following criteria for choosing tornado ''proximity'' soundings: 1) the tornado must have been between 15 min prior to and 105 min after the sonde launch, 2) the tornado must have been within 50 statute miles of the launch site, and 3) the sonde must have been launched in the air mass that produced the tornadic storm. Even with these relatively strict criteria, the findings of Brooks et al. (1994b) and Markowski et al. (1998) suggest that one still cannot be certain that the sonde sampled the actual storm environment, owing to environmental variability. Or, stated another way, environments are inhomogeneous, and no single strand of observations can define them. In the present study, of the 30 ''best proximity'' soundings obtained for the tornadic and nontornadic cases (these were chosen to be as close

TABLE 5. Mean thermodynamic values (std dev in parentheses) in RFDs at the time of tornadogenesis or tornadogenesis failure. The words ''within 4 km'' and ''within 2 km'' refer to the region within a 4-km and 2-km radius *within the RFD*, respectively, of the tornado or mesocyclone center. Only analyses within 5 min of tornadogenesis or tornadogenesis failure, and analyses in which observations were available in at least three of four quadrants (as defined in section 2), are included in the calculation of the means (10 nontornadic cases, 9 tornadic cases). The *P* values are the probabilities that the mean variables in the nontornadic and tornadic cases are the same, and all *P* values were computed using the Multi-Response Permutation Procedure technique described in Mielke et al. (1981). The *P* values that are smaller than 0.001 appear as 0.001. CAPE has been integrated to only 500 mb. Units of θ_v' and θ_e' are in K, units of z_o are in km, units of CAPE and CIN are in J kg^{-1}, units of $\nabla_h\theta_v'$ are in K km^{-1}, and units of p' are in mb.

	Nontornadic	Tornadic	*P* value
Min θ_v' within 4 km	−7.5 (2.6)	−3.2 (1.9)	0.001
Max θ_v' within 2 km	−3.8 (1.4)	−0.7 (1.2)	0.001
Min θ_e' within 4 km	−12.2 (5.7)	−7.0 (5.9)	0.089
Max θ_e' within 2 km	−4.9 (4.4)	−1.7 (1.6)	0.011
Min z_o within 2 km	1.5 (1.0)	0.5 (0.4)	0.057
Max z_o within 4 km	2.4 (1.3)	1.3 (0.4)	0.060
Min CAPE within 4 km	103 (110)	411 (293)	0.006
Max CAPE within 2 km	355 (266)	651 (283)	0.059
Min CIN within 2 km	245 (308)	33 (58)	0.032
Max CIN within 4 km	564 (313)	205 (291)	0.017
Max $\nabla_h\theta_v'$ within RFD	2.5 (1.8)	2.0 (1.9)	0.677
Max p' within RFD	1.7 (1.1)	1.9 (2.2)	0.857

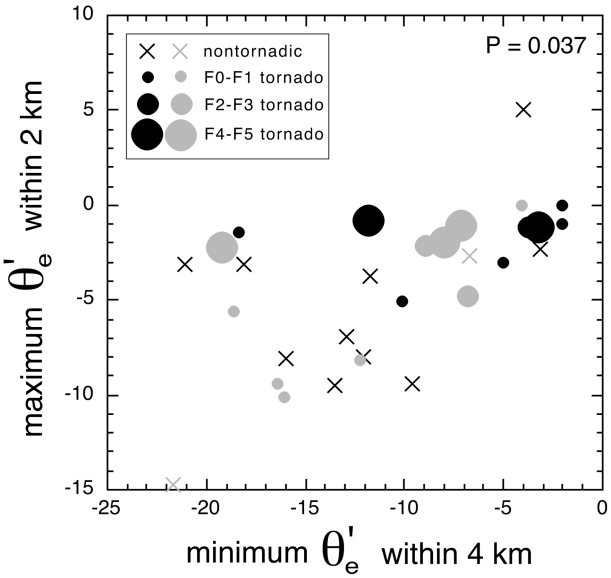

FIG. 12. As in Fig. 11 but maximum θ_e' vs minimum θ_e' values are shown.

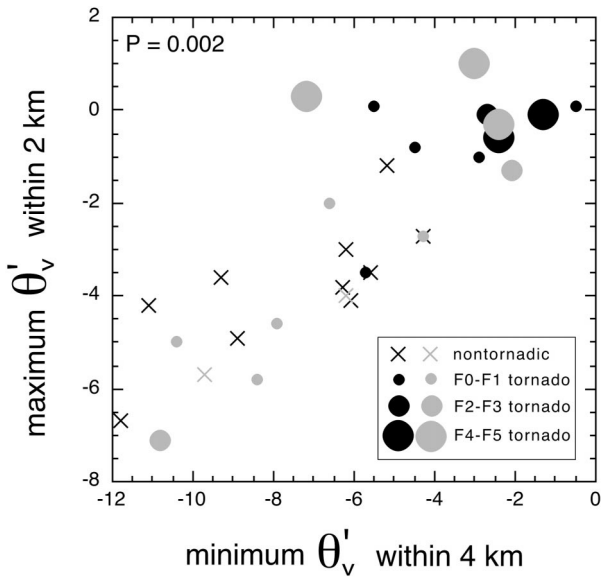

FIG. 11. Scatterplot of maximum θ_v' vs minimum θ_v' values within the RFDs. Black (gray) symbols refer to cases in which analyses were (not) obtained within 5 min of tornadogenesis or tornadogenesis failure, and observations were (not) obtained in at least three of four quadrants (see section 2). Units are K. The *P* value displayed is the probability that the RFDs associated with nontornadic and tornadic supercells contain the same θ_v' characteristics. The *P* value was computed (using the Mielke et al. technique for bivariate data) by only including the analyses obtained within 5 min of tornadogenesis or tornadogenesis failure that contained surface observations in at least three of four quadrants.

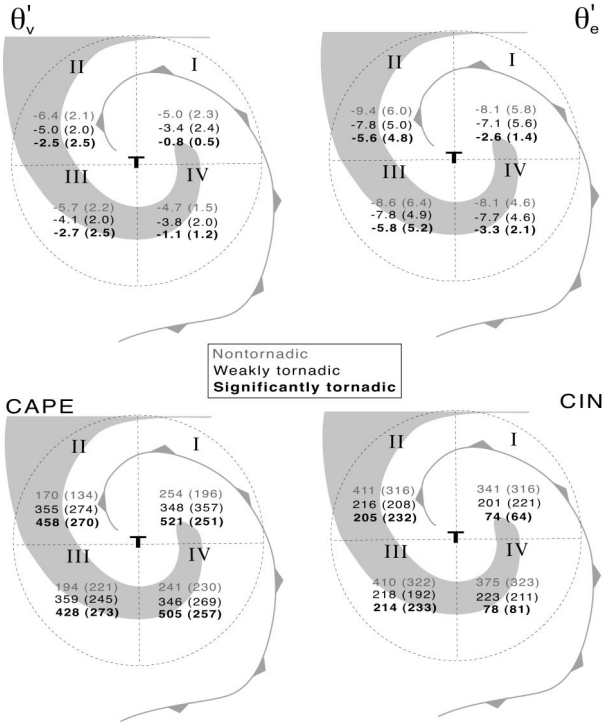

FIG. 13. Mean θ_v', θ_e', CAPE, and CIN values by quadrant (refer to Fig. 2) are shown for nontornadic (gray text), ''weakly tornadic'' (producing F0–F1 tornadoes for ≤5 min; black text), and ''significantly tornadic'' (producing long-lived F0–F1 tornadoes or ≥F2 tornadoes; bold black text) supercells. Standard deviations are included in parentheses.

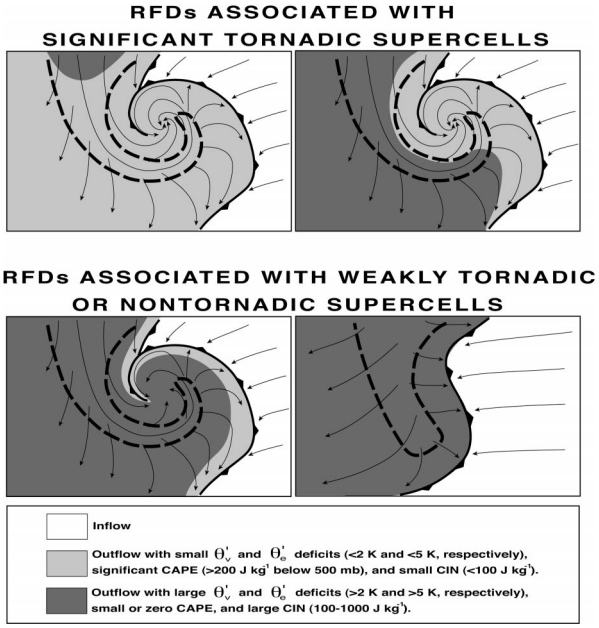

FIG. 14. Composite diagram illustrating the general characteristics of RFDs associated with supercells that produce ''significant'' (e.g., F2 or stronger, or F0–F1 persisting >5 min) tornadoes vs RFDs associated with nontornadic supercells or those that produce weak, brief tornadoes. The thick, dashed contour is the outline of the hook echo, and thin, solid arrows represent idealized streamlines. In the bottom two depictions, the illustration on the left was representative of 11 of 12 tornadogenesis failures, while the illustration on the right depicts an evolution that was observed in only one nontornadic case.

in space and time as possible to tornadogenesis or tornadogenesis failure, and those with wind data were selected over those with missing wind data), only 12 met the criteria put forth by Darkow and his collaborators.[10]

The correlations between θ_v' and θ_e' values within the RFDs and the assorted environmental data are listed in Table 6. The correlations derived from the soundings should be viewed with great caution, owing to the dearth of sounding data used to compute the correlations (by comparison, most severe storms forecasting parameter climatologies include hundreds of soundings), in addition to representativeness issues. In this small sample, there seems to be some tendency for θ_v and θ_e values to be negatively correlated with the storm-relative winds and vertical wind shear in roughly the 2–4-km layer (i.e., θ_v and θ_e deficits seem to be positively correlated with the storm-relative winds and shear).[11] The most significant correlations (r) were between θ_v' (minimum values within 4 km of the circulation centers) and the 3-km storm-relative wind ($r = -0.57$), and θ_e' (minimum values within 4 km of the circulation centers) and the 4-km storm-relative wind ($r = -0.68$). It is possible that the larger storm-relative winds in this layer lead to more substantial entrainment, thus promoting the generation of substantial θ_v and θ_e deficits within the RFDs. Our confidence in the above result is low, however, because of the volatility of storm-relative winds, due to both updraft motion changes and uncertainties in diagnosing storm motion, in addition to the sample size limitations. Nonetheless, it may be worthwhile to examine hodographs in the 2–4-km layer in search of differences between tornadic and nontornadic environments in an expanded study. Previous studies have either investigated storm-relative winds within this layer in only tornadic supercells (e.g., Darkow 1969; Maddox 1976; Darkow and McCann 1977), or they have compared storm-relative winds between tornadic and nontornadic supercells at levels above or below the 2–4-km layer (e.g., Rasmussen and Blanchard 1998; Thompson 1998; Thompson and Edwards 2000).

The correlations between $T_{dd_{\mathrm{sfc}}}$ values and RFD properties perhaps should be viewed as more robust than the above relationship between hodograph and RFD characteristics, due to the fact that inflow $T_{dd_{\mathrm{sfc}}}$ measurements were available in all 30 cases and representativeness is less questionable (Table 6). The correlations also are possibly more encouraging from a forecasting perspective, because surface data are available more frequently in space and time than sounding data. Apparently there is some tendency for relatively humid inflow conditions to be associated with RFDs containing relatively small θ_v deficits (Fig. 15). The correlation between minimum θ_v' (within 4 km of the circulation centers) and $T_{dd_{\mathrm{sfc}}}$ was -0.65. This finding is consistent with the finding by Rasmussen and Blanchard (1998) that low lifting condensation level (LCL) heights increase the likelihood of supercells being tornadic. (For these 30 cases, the mean $T_{dd_{\mathrm{sfc}}}$ in tornadic environments was 5.7 K, and the mean $T_{dd_{\mathrm{sfc}}}$ in nontornadic environments was 8.9 K.) Surface θ_e deficits within RFDs, however, were virtually uncorrelated with inflow $T_{dd_{\mathrm{sfc}}}$ values. This may not be a surprising result, if indeed the inflow relative humidity is related to evaporation potential within the hook echo, because θ_e is approximately conserved during evaporation. Other environmental parameters, for example, maximum T_{dd} below 4 km, 0–6-km shear, 3–6-km shear, and 6-km storm-relative wind had small correlations with the surface RFD characteristics ($|r| < 0.3$ generally).

5. Conclusions

The objectives of this paper were twofold: 1) document the surface thermodynamic fields in the proximity of tornadic and nontornadic low-level mesocyclones; 2) determine if differences exist at the surface in the hook echoes and RFDs of tornadic and nontornadic super-

[10] The criteria used by Darkow (1969) were modified to allow ''tornadogenesis failure'' to replace ''tornado'' in the nontornadic cases.

[11] Vertical wind shear and storm-relative wind correlations above 6 km are not shown because only six of the proximity soundings contained wind data above 6 km. Many of the mobile soundings launched during VORTEX and subsequent experiments lost wind data in the middle and upper troposphere near storms due to the strong electric fields.

TABLE 6. Linear correlations between θ_v and θ_e values in the RFDs analyzed and assorted mean environmental parameters that were suspected of possibly affecting θ_v and θ_e values within RFDs. ''Shear'' refers to the magnitude of the shear vector over the layer indicated. Only soundings satisfying Darkow's (1969) proximity sounding criteria were included in the calculations. The values of $T_{dd\,sfc}$ were obtained from surface stations as described in the text, rather than from soundings.

	Min θ_v' within 4 km	Max θ_v' within 2 km	Min θ_e' within 4 km	Max θ_e' within 2 km
$T_{dd\,sfc}$	−0.65	−0.55	0.07	0.03
Max T_{dd} below 4 km	−0.30	−0.10	−0.21	0.15
0–6-km shear	0.25	0.31	0.03	0.01
2–4-km shear	−0.39	−0.33	−0.34	−0.51
3–6-km shear	0.17	0.31	−0.50	−0.27
2-km storm-relative wind	−0.34	−0.38	0.25	−0.14
3-km storm-relative wind	−0.57	−0.49	−0.56	−0.19
4-km storm-relative wind	−0.34	−0.18	−0.68	−0.28
6-km storm-relative wind	0.01	−0.01	−0.17	−0.24
2–4-km mean storm-relative wind	−0.46	−0.37	−0.50	−0.21
3–6-km mean storm-relative wind	−0.09	0.16	−0.51	−0.05

cells. Given the prior emphasis on the RFD in the tornadogenesis process and the apparent consensus that RFD air parcels enter the tornado, the study naturally was interested in the buoyancy, buoyancy gradients, and potential buoyancy within hook echoes and RFDs—is there something thermodynamically special about RFDs associated with tornadoes compared to ''ordinary'' thunderstorm downdrafts and RFDs associated with nontornadic supercells?

Evidence was presented in support of the following conclusions:

1) Tornado likelihood, intensity, and longevity increase as the surface buoyancy, potential buoyancy (CAPE), and equivalent potential temperature in the RFD increase, and as the CIN associated with RFD parcels at the surface decreases.

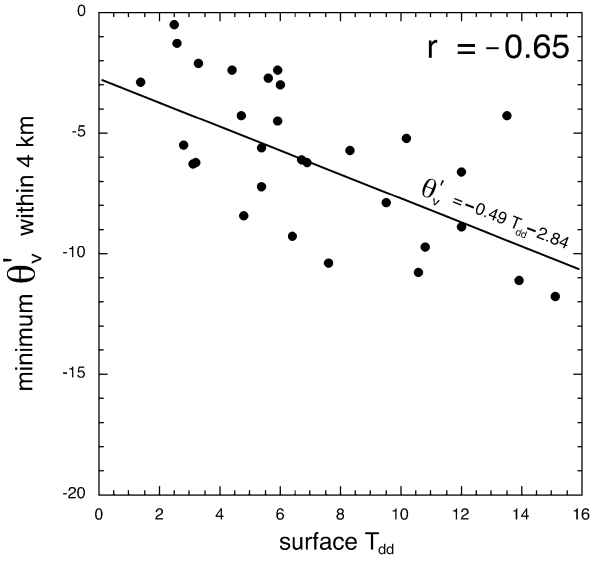

FIG. 15. Scatterplot of minimum θ_v' values vs surface T_{dd} values for the 30 cases. The linear correlation appears at the top right and a best-fit line has been added.

2) The presence of a circulation at the surface is not a sufficient condition for tornadogenesis.
3) Baroclinity at the surface within the hook echo is not a necessary condition for tornadogenesis.

The final four conclusions are more tentative:

1) Evaporative cooling and entrainment of midlevel potentially cold air play smaller roles in the formation of RFDs associated with tornadic supercells compared to nontornadic supercells.
2) The presence of surface-based CAPE in the RFD is a necessary condition for tornadogenesis.
3) Most nontornadic supercells contain circulations at the surface.
4) The ambient relative humidity profile, at least at low levels, is associated with the coldness of RFDs; environments characterized by high boundary layer relative humidity (and low cloud base) are more conducive to RFDs associated with relatively high buoyancy than environments characterized by low boundary layer relative humidity (and high cloud base).

It should be emphasized that while relatively warm, moist, and potentially buoyant RFD air parcels appear to be necessary for the genesis of significant tornadoes, this condition is not sufficient for tornadogenesis. Additional factors are almost certainly important (e.g., surface roughness and the angular momentum distribution through which the RFD descends).

We hope to present idealized simulation results in a separate paper in order to provide a possible physical explanation for the observed association among relatively warm, moist downdrafts, tornadogenesis, and high boundary layer relative humidity. In the future it may be worthwhile to seek possible ways of inferring RFD characteristics from radar data in addition to environmental data, because radar data are so readily available in real time and it is now known that tornadoes occur over a wide range of mesocyclone strengths.

Acknowledgments. We are grateful to all VORTEX volunteers (too numerous to mention). We also thank Robert Carver for computing assistance and Al Pietrycha for running quality-control checks on the 1998 mobile mesonet data. Tom Shepherd, Mike Magsig, and Scott Stephens also are acknowledged for helping to obtain hard-to-find radar data, and we thank Mark Shafer for speedy fulfillment of Oklahoma Mesonet data requests. Dr. Bill Winn provided 8 June 1995 turtle data and Dr. David Blanchard provided some needed FORTRAN code. Tim Marshall generously provided some helpful video footage. Thanks also are extended to Drs. Bob Davies-Jones, Chuck Doswell, Fred Carr, and Brian Fiedler, who reviewed earlier versions of this work, and to three anonymous reviewers. NSF Grant ATM-9617318 supported much of this research.

APPENDIX

Error Analysis

The errors of mobile mesonet temperature (T), pressure (p), and relative humidity (h) measurements are documented by Straka et al. (1996). In this appendix, the errors associated with the derived variables of reduced pressure, virtual and equivalent potential temperature fluctuations, dewpoint temperature, parcel origin height, convective available potential energy (CAPE), and convective inhibition (CIN) are estimated.

a. Reduced pressure errors

Level 2 Digital Elevation Model (DEM) accuracy, $\delta z'$, is within one-half contour interval on a 7.5′ quadrangle map (U.S. Department of the Interior 1992). This corresponds to 2.5 ft (0.78 m) on the ''high plains'' of the United States (west of ~101°W) and to 5 ft (1.6 m) on the ''low plains'' (east of ~101°W). Comparisons at random locations with elevation values obtained directly from U.S. Geological Survey 7.5′ topographic maps revealed slightly better accuracy.

GPS uncertainty in the horizontal positions of mobile mesonet observations was approximately 100 m. Tests were performed at 100 random locations on the high plains and at 100 random locations on the low plains to ascertain the elevation uncertainty owing to the uncertainty in position, $\delta z''$. On the high plains, the rms elevation error ($\delta z''$) was 1.1 m (obtained by using the largest elevation differences at all points within 100 m of the 100 randomly chosen reference positions). On the low plains, the RMS elevation error was 3.8 m.

The total elevation uncertainty, δz, can be estimated as

$$\delta z = [(\delta z')^2 + (\delta z'')^2]^{1/2}. \quad \text{(A1)}$$

On the high plains,

$$\delta z \approx [(0.78 \text{ m})^2 + (1.1 \text{ m})^2]^{1/2} \approx 1.3 \text{ m}, \quad \text{(A2)}$$

and on the low plains,

$$\delta z \approx [(1.6 \text{ m})^2 + (3.8 \text{ m})^2]^{1/2} \approx 4.1 \text{ m}. \quad \text{(A3)}$$

Pressure was reduced to the average height of the vehicle observations using the integrated hydrostatic equation of the form

$$p = p_{\text{obs}} \exp\left[\frac{(z - \overline{z})g}{R_d \overline{T}_v}\right], \quad \text{(A4)}$$

where $\overline{z}$ is the average elevation of the mobile mesonet observations within the analysis domain, p is the pressure reduced to $\overline{z}$, p_{obs} is the pressure observed by the mobile mesonet vehicle, z is the elevation at which the mobile mesonet pressure p_{obs} was recorded, R_d is the gas constant for dry air, and $\overline{T}_v$ is approximated as the average virtual temperature (liquid water effects neglected) recorded by the mobile mesonet within the analysis domain.

The uncertainty of a reduced pressure measurement (δp) owing to elevation errors (δz) and instrument errors (δp_{obs}), assuming that the elevation and instrument errors are independent and random, is

$$\delta p = \left[\left(\frac{\partial p}{\partial p_{\text{obs}}}\delta p_{\text{obs}}\right)^2 + \left(\frac{\partial p}{\partial z}\delta z\right)^2 + (\delta\psi)^2\right]^{1/2} \quad \text{(A5)}$$

following Taylor (1982), where the uncertainty of $\overline{z}$ ($\delta\overline{z}$) has been assumed to be zero, and the effect on reduced p values owing to errors in $\overline{T}_v$ is not considered because it is small. The last term on the right side of (A5) has been added in a purely ad hoc manner to account for the subjective analysis uncertainty in regions where observations are sparse. This term is arbitrarily modeled as

$$\delta\psi = |\nabla p| \cdot 0.5 \text{ km}, \quad \text{(A6)}$$

where the factor 0.5 km is multiplied to the magnitude of the pressure gradient in the region of interest with the justification being that $\delta\psi$ is then equal to roughly one-half of a contour interval where the interval is chosen so that the average contour spacing is approximately 1 km. For example, if a weak pressure gradient exists [$|\nabla p| = 1$ mb (5 km)$^{-1}$], then the uncertainty owing to the subjective contour analysis would be estimated to be 0.1 mb.

Because

$$\frac{\partial p}{\partial p_{\text{obs}}} = \exp\left[\frac{(z - \overline{z})g}{R_d \overline{T}_v}\right] = \frac{p}{p_{\text{obs}}} \approx 1, \quad \text{and} \quad \text{(A7)}$$

$$\frac{\partial p}{\partial z} = \frac{pg}{R_d \overline{T}_v}, \quad \text{(A8)}$$

(A5) can be written as

$$\delta p = \left[(\delta p_{\text{obs}})^2 + \left(\frac{pg}{R_d \overline{T}_v}\delta z\right)^2 + (\delta\psi)^2\right]^{1/2}. \quad \text{(A9)}$$

Assuming $p \approx 950$ mb and $\overline{T}_v \approx 300$ K, substituting $\delta p_{\text{obs}} = 0.6$ mb (Straka et al. 1996), and neglecting $\delta\psi$,

the uncertainty of a pressure measurement owing to elevation errors (owing to both DEM and GPS position errors) and instrument errors is estimated to be approximately

$$\delta p \approx 0.62 \text{ mb} \quad \text{on high plains} \quad (\delta z = 1.3 \text{ m}) \tag{A10}$$

$$\delta p \approx 0.75 \text{ mb} \quad \text{on low plains} \quad (\delta z = 4.1 \text{ m}). \tag{A11}$$

Furthermore, because $p' = p - \overline{p}$, it can be shown that

$$\delta p' = [(\delta p)^2 + (\delta \overline{p})^2]^{1/2}, \tag{A12}$$

where $\delta p'$ and $\delta \overline{p}$ are the uncertainties of the fluctuation and base state pressure, respectively. In other words, additional uncertainty (and perhaps the largest amount) is introduced by misspecification of the base-state pressure when pressure fluctuations are analyzed.

It is difficult to quantify the error associated with the estimation of the base state, since no theoretically justifiable means exists for defining the base state in a network of spatially and temporally discrete observations. The method for estimating the base state is described in section 2. If N observations are available within a 400-km radius to estimate the base state (where $\overline{p} = \Sigma_{i=1}^{N} w_i p_i / \Sigma_{i=1}^{N} w_i$), then the uncertainty of the base state, $\delta \overline{p}$, can be crudely represented by the sensitivity of $\overline{p}$ to the choice of κ that appears in w_i. Thus, we arbitrarily define the base-state pressure uncertainty to be

$$\delta \overline{p} = \max(|\overline{p}_{\kappa_1} - \overline{p}_{\kappa_o}|, |\overline{p}_{\kappa_2} - \overline{p}_{\kappa_o}|), \tag{A13}$$

where $\delta \overline{p}$is taken to be the larger of the differences between the weighted average of observations using κ_1 ($=0.5\kappa_o$) and κ_o and the weighted average of observations using κ_o and κ_2 ($=1.5\kappa_o$).

b. Virtual potential temperature fluctuation errors

Errors in pressure, temperature, and relative humidity observations are accompanied by errors in computed values of virtual potential temperature fluctuations. The inaccuracies of these measurements are approximately 0.6 mb, 0.3–0.5 K (''fast'' versus ''slow'' temperature), and <5%, respectively (Straka et al. 1996). Furthermore, errors in the parameterization of q_l in terms of the radar reflectivity factor as well as misspecification of the base state also adversely affect computations of virtual potential temperature fluctuations. In this section, the error associated with buoyancy calculations also is included in the investigation

The total buoyancy, B, neglecting ice, can be expressed as

$$B = g\frac{\theta_v'}{\overline{\theta}_v} = g\left(\frac{\theta'}{\overline{\theta}} + 0.61 q_v' - q_l\right), \tag{A14}$$

where (θ_v') θ' is the (virtual) potential temperature fluctuation, ($\overline{\theta}_v$) $\overline{\theta}$ is the base-state (virtual) potential temperature, q_v' is the water vapor mixing ratio fluctuation, and q_l is the liquid water mixing ratio. If the uncertainties of θ_v' and $\overline{\theta}_v$ are independent and random, then the uncertainty of the buoyancy calculation, δB, is

$$\delta B = \left[\left(\frac{\partial B}{\partial \theta_v'}\delta\theta_v'\right)^2 + \left(\frac{\partial B}{\partial \overline{\theta}_v}\delta\overline{\theta}_v\right)^2 + (\delta\psi)^2\right]^{1/2}, \tag{A15}$$

where $\delta\theta_v'$ and $\delta\overline{\theta}_v$ are the uncertainties of θ_v' and $\overline{\theta}_v$, and $\delta\psi$ has been added in an ad hoc manner similar to the previous section to account for the subjective analysis uncertainty [$\delta\psi$ may be modeled using a form similar to (A6)]. The $\delta\psi$ term will be excluded in the analysis hereafter; it should be remembered that in regions where observations are sparse, such that subjective analysis of the meteorological fields is required, this term is estimated and included in the uncertainty analyses that appear in the main body of the text.

We can simplify (A15) as

$$\delta B = \left[\left(\frac{g}{\overline{\theta}_v}\delta\theta_v'\right)^2 + \left(-\frac{B}{\overline{\theta}_v}\delta\overline{\theta}_v\right)^2\right]^{1/2}. \tag{A16}$$

It is desirable to express $\delta\theta_v'$ in terms of δT, δp, and δh. By definition,

$$\theta_v' = T_v\left(\frac{p_o}{p}\right)^{\kappa} - \overline{\theta}_v = T(1 + 0.61 q_v)\left(\frac{p_o}{p}\right)^{\kappa} - \overline{\theta}_v, \tag{A17}$$

where $\theta_v = \overline{\theta}_v + \theta_v'$, T_v is the virtual temperature, $p_0 = 1000$ mb, and $\kappa = R_d/c_p$, where c_p is the specific heat of dry air at constant pressure. The effect of liquid water loading errors has been neglected here. The errors of the parameterization cannot be quantified easily, and errors arising from reflectivity ''errors'' (q_l is parameterized from the reflectivity) due to range-dependent resolution volume differences from case to case are expected to be less than 0.25 K at reflectivities <45 dBZ.

From (A17), we can express the uncertainty of θ_v' (assuming T, p, q_v, and $\overline{\theta}_v$ errors are independent and random) as

$$\delta\theta_v' = \left[\left(\frac{\partial\theta_v'}{\partial T}\delta T\right)^2 + \left(\frac{\partial\theta_v'}{\partial p}\delta p\right)^2 + \left(\frac{\partial\theta_v'}{\partial q_v}\delta q_v\right)^2 + \left(\frac{\partial\theta_v'}{\partial\overline{\theta}_v}\delta\overline{\theta}_v\right)^2\right]^{1/2} \tag{A18}$$

$$= \left[\left(\frac{\theta_v}{T}\delta T\right)^2 + \left(-\frac{\kappa\theta_v}{p}\delta p\right)^2 + (0.61\theta\delta q_v)^2 + (\delta\overline{\theta}_v)^2\right]^{1/2}. \tag{A19}$$

But

$$q_v = hq_s \approx \frac{6.112h\varepsilon}{p}\exp\left(\frac{17.67T}{T + 243.5}\right), \quad \text{(A20)}$$

where q_s is the saturation mixing ratio and has been approximated using the formula presented in Bolton (1980), ε (=0.622) is the ratio of the gas constants of dry air and water vapor, and T is in degrees Celsius. From (A20) the following is obtained:

$$\delta q_v = \left[\left(\frac{\partial q_v}{\partial h}\delta h\right)^{-2} + \left(\frac{\partial q_v}{\partial p}\delta p\right)^2 + \left(\frac{\partial q_v}{\partial T}\delta T\right)^2\right]^{1/2} \quad \text{(A21)}$$

$$= \left\{\left[\frac{6.112\varepsilon}{p}\exp\left(\frac{17.67T}{T + 243.5}\right)\delta h\right]^2 + \left[-\frac{6.112\varepsilon h}{p^2}\exp\left(\frac{17.67T}{T + 243.5}\right)\delta p\right]^2 + \left[\frac{6.112\varepsilon h}{p}\exp\left(\frac{17.67T}{T + 243.5}\right)\frac{17.67 \cdot 243.5}{(T + 243.5)^2}\delta T\right]\right\}^{1/2}. \quad \text{(A22)}$$

Using (A19) and (A22), the total buoyancy uncertainty, δB, can be evaluated. For typical conditions, if we assume θ = 300 K, θ_v = 304 K, $\overline{\theta}_v$ = 303 K, p = 950 mb, T = 296 K, h = 0.45 (corresponds to $q_v \approx$ 0.015), δT = 0.3 K [except where it appears in (A22), because slow temperature (δT = 0.5 K) is used for calculations that depend on moisture], δp = 0.6 mb [only instrument uncertainty affects δp because station p, not reduced p, is used to compute q (in the preceding section, this uncertainty was referred to as δp_{obs})], and δh = 0.03, we obtain

$$\delta\theta_v' \approx [(0.34\text{ K})^2 + (\delta\overline{\theta}_v)^2]^{1/2} \quad \text{and} \quad \text{(A23)}$$

$$\delta B \approx [(0.011\text{ m s}^{-2})^2 + (0.033\text{ m s}^{-2}\text{ K}^{-1}\,\delta\overline{\theta}_v)^2]^{1/2}, \quad \text{(A24)}$$

where $\delta\overline{\theta}_v$ is modeled in a manner identical to $\delta\overline{p}$.

c. Errors associated with other derived quantities

If we use Bolton's (1980) formula for vapor pressure, then the following expression for the dewpoint temperature (°C) may be obtained:

$$T_d = \frac{243.5\ln\left(\frac{pq_v}{6.112\varepsilon}\right)}{17.67 - \ln\left(\frac{pq_v}{6.112\varepsilon}\right)}, \quad \text{(A25)}$$

where p is in millibars and q_v is in grams per gram. If p and q_v errors are independent and random, then the uncertainty associated with the calculation of the dewpoint temperature may be estimated as

$$\delta T_d = \left[\left(\frac{\partial T_d}{\partial p}\delta p\right)^2 + \left(\frac{\partial T_d}{\partial q_v}\delta q_v\right)^2\right]^{1/2} = \left\{\left[\left(\frac{\delta p}{p}\right)^2 + \left(\frac{\delta q_v}{q_v}\right)^2\right]\left[\frac{T_d + 243.5}{17.67 - \ln\left(\frac{pq_v}{6.112\varepsilon}\right)}\right]^2\right\}^{1/2} \approx 0.75\text{ K}, \quad \text{(A26)}$$

when p = 950 mb, T_d = 20°C, q_v = 0.015, $\delta q_v = 7 \times 10^{-4}$ [obtained from (A22)], and δp = 0.6 mb are used.

Equivalent potential temperature (θ_e) also was computed using the formulation by Bolton (1980). Using (6), the uncertainty of θ_e fluctuations (θ_e') can be expressed as

$$\delta\theta_e' = [(\delta\theta_e)^2 + (\delta\overline{\theta}_e)^2]^{1/2} \quad \text{(A27)}$$

$$= \left[\left(\frac{\partial\theta_e}{\partial T}\delta T\right)^2 + \left(\frac{\partial\theta_e}{\partial p}\delta p\right)^2 + \left(\frac{\partial\theta_e}{\partial q_v}\delta q_v\right)^2 + \left(\frac{\partial\theta_e}{\partial T^*}\delta T^*\right)^2 + (\delta\overline{\theta}_e)^2\right]^{1/2}, \quad \text{(A28)}$$

where T^* is the temperature at the saturation point of the air parcel and

$$\frac{\partial\theta_e}{\partial T} = \frac{\theta_e}{T}\left\{1 - \frac{3.5}{T^{*2}}\left[q_v(1 + 0.81q_v)\left(\frac{3376}{T^*} - 2.54\right)\right]\right\} \quad \text{(A29)}$$

$$\frac{\partial\theta_e}{\partial p} = -0.2854(1 - 0.28q_v)\frac{\theta_e}{p} \quad \text{(A30)}$$

$$\frac{\partial\theta_e}{\partial q_v} = \theta_e\left[\ln\left(\frac{p_o}{p}\right) + (1 + 1.62q_v)\left(\frac{3376}{T^*} - 2.54\right)\right] \quad \text{(A31)}$$

$$\frac{\partial\theta_e}{\partial T^*} = -\frac{\theta_e}{T^{*2}}[3376q_v(1 + 0.81q_v)]. \quad \text{(A32)}$$

Given the known errors for temperature and relative humidity (Straka et al. 1996), $\delta T^* \approx 0.5$ K for typical conditions. For $T = 300$ K, $p = 950$ mb, and $\theta_e = 350$ K, $\delta\theta_e \approx 2.3$ K. The component of the uncertainty owing to uncertainty of the base state, $\delta\overline{\theta}_e$, was modeled in the same way that $\delta\overline{p}$ and $\delta\overline{\theta}_v$ were modeled.

The uncertainty of the height from which a surface parcel of air has descended (assuming that θ_e has been approximately conserved) depends on the potential instability; that is, as $|\partial\theta_e/\partial z|$ increases, the origin of the air parcel that has reached the surface becomes more certain. The uncertainty of the height from which a surface parcel has descended, δz_o (where the ''o'' subscript denotes origin), can be written as

$$\delta z_o = \left|\frac{\partial\theta_e}{\partial z}\right|^{-1} \delta\theta_e, \qquad \text{(A33)}$$

where $\partial\theta_e/\partial z$ is evaluated at z_o. Using $\delta\theta_e \approx 2.3$, δz_o ranges from ~500 m for large [(5 K) km^{-1}] magnitudes of $\partial\theta_e/\partial z$ to ~1 km for small [(2 K) km^{-1}] magnitudes of $\partial\theta_e/\partial z$.

Finally, the propagation of T, T_d, and p errors into CAPE and CIN calculations also depends on the vagaries of the sounding. These errors were evaluated numerically on a case-by-case basis by perturbing surface parcels by the δT, δT_d, and δp values obtained previously. The effects of sounding representativeness errors on CAPE and CIN calculations could not reasonably be quantified, but it is believed that thermodynamic measurement errors at the surface are the largest contributor to CAPE and CIN errors.

REFERENCES

Adlerman, E. J., K. K. Droegemeier, and R. P. Davies-Jones, 1999: A numerical simulation of cyclic mesocyclogenesis. *J. Atmos. Sci.*, **56,** 2045–2069.

Barnes, S. L., 1964: A technique for maximizing details in numerical weather map analysis. *J. Appl. Meteor.*, **3,** 396–409.

——, 1978a: Oklahoma thunderstorms on 29–30 April 1970. Part I: Morphology of a tornadic storm. *Mon. Wea. Rev.*, **106,** 673–684.

——, 1978b: Oklahoma thunderstorms on 29–30 April 1970. Part II: Radar-observed merger of twin hook echoes. *Mon. Wea. Rev.*, **106,** 685–696.

Beebe, R. G., 1959: Notes on the Scottsbluff, Nebraska tornado, 27 June 1955. *Bull. Amer. Meteor. Soc.*, **40,** 109–116.

Betts, A. K., 1982: Saturation point analysis of moist convective overturning. *J. Atmos. Sci.*, **39,** 1484–1505.

Blanchard, D. O., and R. E. Lopez, 1985: Spatial patterns of convection in south Florida. *Mon. Wea. Rev.*, **113,** 1282–1299.

——, and J. M. Straka, 1998: Some possible mechanisms for tornadogenesis failure in a supercell. Preprints, *19th Conf. on Severe Local Storms,* Minneapolis, MN, Amer. Meteor. Soc., 116–119.

Bluestein, H. B., 1983: Surface meteorological observations in severe thunderstorms. Part II: Field experiments with TOTO. *J. Climate Appl. Meteor.*, **22,** 919–930.

Bohren, C. F., and B. A. Albrecht, 1998: *Atmospheric Thermodynamics.* Oxford University Press, 402 pp.

Bolton, D., 1980: The computation of equivalent potential temperature. *Mon. Wea. Rev.*, **108,** 1046–1053.

Brandes, E. A., 1977a: Flow in a severe thunderstorm observed by dual-Doppler radar. *Mon. Wea. Rev.*, **105,** 113–120.

——, 1977b: Gust front evolution and tornado genesis as viewed by Doppler radar. *J. Appl. Meteor.*, **16,** 333–338.

——, 1978: Mesocyclone evolution and tornadogenesis: Some observations. *Mon. Wea. Rev.*, **106,** 995–1011.

——, 1981: Finestructure of the Del City–Edmond tornadic mesocirculation. *Mon. Wea. Rev.*, **109,** 635–647.

——, 1984a: Relationships between radar-derived thermodynamic variables and tornadogenesis. *Mon. Wea. Rev.*, **112,** 1033–1052.

——, 1984b: Vertical vorticity generation and mesocyclone sustenance in tornadic thunderstorms: The observational evidence. *Mon. Wea. Rev.*, **112,** 2253–2269.

Brock, F. V., K. Crawford, R. Elliot, G. Cupernus, S. Stadler, H. Johnson, and M. Eilts, 1995: The Oklahoma Mesonet: A technical overview. *J. Atmos. Oceanic Technol.*, **12,** 5–19.

Brooks, H. E., C. A. Doswell III, and R. P. Davies-Jones, 1993: Environmental helicity and the maintenance and evolution of low-level mesocyclones. *The Tornado: Its Structure, Dynamics, Prediction, and Hazards, Geophys. Monogr.*, No. 79, Amer. Geophys. Union, 97–104.

——, ——, and R. B. Wilhelmson, 1994a: The role of midtropospheric winds in the evolution and maintenance of low-level mesocyclones. *Mon. Wea. Rev.*, **122,** 126–136.

——, ——, and J. Cooper, 1994b: On the environments of tornadic and nontornadic mesocyclones. *Wea. Forecasting*, **9,** 606–618.

Brown, J. M., and K. R. Knupp, 1980: The Iowa cyclonic–anticyclonic tornado pair and its parent thunderstorm. *Mon. Wea. Rev.*, **108,** 1626–1646.

Browning, K. A., and F. H. Ludlam, 1962: Airflow in convective storms. *Quart. J. Roy. Meteor. Soc.*, **88,** 117–135.

——, and R. J. Donaldson, 1963: Airflow and structure of a tornadic storm. *J. Atmos. Sci.*, **20,** 533–545.

Burgess, D. W., R. A. Brown, L. R. Lemon, and C. R. Safford, 1977: Evolution of a tornadic thunderstorm. Preprints, *10th Conf. on Severe Local Storms,* Omaha, NE, Amer. Meteor. Soc., 84–89.

Charba, J., and Y. Sasaki, 1971: Structure and movement of the severe thunderstorms of 3 April 1964 as revealed from radar and surface mesonetwork data analysis. *J. Meteor. Soc. Japan,* **49,** 191–214.

Darkow, G. L., 1969: An analysis of over sixty tornado proximity soundings. Preprints, *Sixth Conf. on Severe Local Storms,* Chicago, IL, Amer. Meteor. Soc., 218–221.

——, and D. W. McCann, 1977: Relative environmental winds for 121 tornado bearing storms. Preprints, *10th Conf. on Severe Local Storms,* Omaha, NE, Amer. Meteor. Soc., 413–417.

Daugherty, J. R., A. I. Watson, T. R. Shepherd, and C. L. Ziegler, 1996: The evolution of tornadic supercells during VORTEX-95 as observed by the NOAA P-3 lower-fuselage C-band radar. Preprints, *18th Conf. on Severe Local Storms,* San Francisco, CA, Amer. Meteor. Soc., 128–132.

Davies-Jones, R. P., 2000: Can the hook echo instigate tornadogenesis barotropically? Preprints, *20th Conf. on Severe Local Storms,* Orlando, FL, Amer. Meteor. Soc., 269–272.

——, and H. E. Brooks, 1993: Mesocyclogenesis from a theoretical perspective. *The Tornado: Its Structure, Dynamics, Prediction, and Hazards, Geophys. Monogr.*, No. 79, Amer. Geophys. Union, 105–114.

Emanuel, K. A., 1994: *Atmospheric Convection.* Oxford University Press, 580 pp.

Forbes, G. S., 1978: Three scales of motion associated with tornadoes. Nuclear Regulatory Commission Rep. CR-0363, 359 pp. [NTIS PB288291.]

——, 1981: On the reliability of hook echoes as tornado indicators. *Mon. Wea. Rev.*, **109,** 1457–1466.

Fujita, T. T., 1955: Results of detailed synoptic studies of squall lines. *Tellus,* **4,** 405–436.

——, 1958: Tornado cyclone: Bearing system of tornadoes. *Proc. Seventh Conf. on Radar Meteorology,* Miami Beach, FL, Amer. Meteor. Soc., K31–K38.

——, 1963: Analytical mesometeorology: A review. *Severe Local Storms, Meteor. Monogr.,* No. 27, Amer. Meteor. Soc., 77–125.
——, 1975: New evidence from the April 3–4, 1974 tornadoes. Preprints, *Ninth Conf. on Severe Local Storms,* Norman, OK, Amer. Meteor. Soc., 248–255.
——, and R. M. Wakimoto, 1982: Anticyclonic tornadoes in 1980 and 1981. Preprints, *12th Conf. on Severe Local Storms,* San Antonio, TX, Amer. Meteor. Soc., 213–216.
——, M. R. Hjelmfelt, and S. A. Changnon, 1977: Mesoanalysis of record Chicago rainstorm using radar, satellite, and rainguage data. Preprints, *10th Conf. on Severe Local Storms,* Omaha, NE, Amer. Meteor. Soc., 65–72.
Gal-Chen, T., 1978: A method for the initialization of the anelastic equations: Implications for matching models with observations. *Mon. Wea. Rev.,* **106,** 587–606.
Garrett, R. A., and V. D. Rockney, 1962: Tornadoes in northeastern Kansas, May 19, 1960. *Mon. Wea. Rev.,* **90,** 231–240.
Gilmore, M. S., and L. J. Wicker, 1998: The influence of midtropospheric dryness on supercell morphology and evolution. *Mon. Wea. Rev.,* **126,** 943–958.
Glickman, T., Ed., 2000: *Glossary of Meteorology.* 2d ed. Amer. Meteor. Soc., 855 pp.
Hane, C. E., and P. S. Ray, 1985: Pressure and buoyancy fields derived from Doppler radar data in a tornadic thunderstorm. *J. Atmos. Sci.,* **42,** 18–35.
——, R. B. Wilhelmson, and T. Gal-Chen, 1981: Retrieval of thermodynamic variables within deep convective clouds: Experiments in three dimensions. *Mon. Wea. Rev.,* **109,** 564–576.
Houze, R. A., Jr., 1993: *Cloud Dynamics.* Academic Press, 573 pp.
Jensen, B., T. P. Marshall, M. A. Mabey, and E. N. Rasmussen, 1983: Storm scale structure of the Pampa storm. Preprints, *13th Conf. on Severe Local Storms,* Tulsa, OK, Amer. Meteor. Soc., 85–88.
Johnson, B. C., 1983: The heat burst of 29 May 1976. *Mon. Wea. Rev.,* **111,** 1776–1792.
Johnson, D. E., P. K. Wang, and J. M. Straka, 1993: Numerical simulations of the 2 August 1981 CCOPE supercell storm with and without ice microphysics. *J. Appl. Meteor.,* **32,** 745–759.
Johnson, K. W., P. S. Ray, B. C. Johnson, and R. P. Davies-Jones, 1987: Observations related to the rotational dynamics of the 20 May 1977 tornadic storms. *Mon. Wea. Rev.,* **115,** 2463–2478.
Jorgensen, D. P., P. H. Hildebrand, and C. L. Frush, 1983: Feasibility test of an airborne pulse-Doppler meteorological radar. *J. Climate Appl. Meteor.,* **22,** 744–757.
Kerr, B. W., and G. L. Darkow, 1996: Storm-relative winds and helicity in the tornadic thunderstorm environment. *Wea. Forecasting,* **11,** 489–505.
Kessler, E., 1969: *On the Distribution and Continuity of Water Substance in Atmospheric Circulations. Meteor. Monogr.,* Amer. Meteor. Soc., No. 32, 84 pp.
Klemp, J. B., and R. Rotunno, 1983: A study of the tornadic region within a supercell thunderstorm. *J. Atmos. Sci.,* **40,** 359–377.
——, R. B. Wilhelmson, and P. S. Ray, 1981: Observed and numerically simulated structure of a mature supercell thunderstorm. *J. Atmos. Sci.,* **38,** 1558–1580.
Koch, S. E., M. DesJardins, and P. J. Kocin, 1983: An interactive Barnes objective map analysis scheme for use with satellite and conventional data. *J. Climate Appl. Meteor.,* **22,** 1487–1503.
Lemon, L. R., 1976: The flanking line, a severe thunderstorm intensification source. *J. Atmos. Sci.,* **33,** 686–694.
Leslie, L. M., and R. K. Smith, 1978: The effect of vertical stability on tornadogenesis. *J. Atmos. Sci.,* **35,** 1281–1288.
Ludlam, F. H., 1963: Severe local storms: A review. *Severe Local Storms, Meteor. Monogr.,* No. 27, Amer. Meteor. Soc., 1–30.
Maddox, R. A., 1976: An evaluation of tornado proximity wind and stability data. *Mon. Wea. Rev.,* **104,** 133–142.
Markowski, P. A. 2002a: Hook echoes and rear-flank downdrafts: A review. *Mon. Wea. Rev.,* **130,** 852–876.
——, 2002b: Mobile mesonet observations on 3 May 1999. *Wea. Forecasting,* **17,** 430–444.
——, J. M. Straka, E. N. Rasmussen, and D. O. Blanchard, 1998: Variability of storm-relative helicity during VORTEX. *Mon. Wea. Rev.,* **126,** 2942–2958.
——, E. N. Rasmussen, and J. M. Straka, 2000: Surface thermodynamic characteristics of RFDs as measured by a mobile mesonet. Preprints, *20th Conf. on Severe Local Storms,* Orlando, FL, Amer. Meteor. Soc., 251–254.
McCaul, E. W., Jr., and M. L. Weisman, 1996: simulations of shallow supercell storms in landfalling hurricane environments. *Mon. Wea. Rev.,* **124,** 408–429.
——, and ——, 2001: The sensitivity of simulated supercell structure and intensity to variations in the shapes of environmental buoyancy and shear profiles. *Mon. Wea. Rev.,* **129,** 664–687.
Mielke, P. W., K. J. Berry, and E. S. Johnson, 1976: Multi-response permutation procedures for a priori classifications. *Commun. Stat. Theor. Methods,* **A5,** 1409–1424.
——, ——, and G. W. Brier, 1981: Application of multi-response permutation procedures for examining seasonal changes in monthly mean sea-level pressure patterns. *Mon. Wea. Rev.,* **109,** 120–126.
Nelson, S. P., 1977: Rear flank downdraft: A hailstorm intensification mechanism. Preprints, *10th Conf. on Severe Local Storms,* Omaha, NE, Amer. Meteor. Soc., 521–525.
Rasmussen, E. N., and J. M. Straka, 1996: Mobile mesonet observations of tornadoes during VORTEX-95. Preprints, *18th Conf. on Severe Local Storms,* San Francisco, CA, Amer. Meteor. Soc., 1–5.
——, and D. O. Blanchard, 1998: A baseline climatology of sounding-derived supercell and tornado forecast parameters. *Wea. Forecasting,* **13,** 1148–1164.
——, R. E. Peterson, J. E. Minor, and B. D. Campbell, 1982: Evolutionary characteristics and photogrammetric determination of windspeeds within the Tulia outbreak tornadoes 28 May 1980. Preprints, *12th Conf. on Severe Local Storms,* San Antonio, TX, Amer. Meteor. Soc., 301–304.
——, J. M. Straka, R. P. Davies-Jones, C. A. Doswell, F. H. Carr, M. D. Eilts, and D. R. MacGorman, 1994: Verification of the Origins of Rotation in Tornadoes Experiment: VORTEX. *Bull. Amer. Meteor. Soc.,* **75,** 995–1006.
Ray, P. S., 1976: Vorticity and divergence fields within tornadic storms from dual-Doppler observations. *J. Appl. Meteor.,* **15,** 879–890.
——, R. J. Doviak, G. B. Walker, D. Sirmans, J. Carter, and B. Bumgarner, 1975: Dual-Doppler observation of a tornadic storm. *J. Appl. Meteor.,* **14,** 1521–1530.
——, B. C. Johnson, K. W. Johnson, J. S. Bradberry, J. J. Stephens, K. K. Wagner, R. B. Wilhelmson, and J. B. Klemp, 1981: The morphology of several tornadic storms on 20 May 1977. *J. Atmos. Sci.,* **38,** 1643–1663.
——, D. P. Jorgensen, and S.-L. Wang, 1985: Airborne Doppler radar observations of a convective storm. *J. Climate Appl. Meteor.,* **24,** 687–698.
Rotunno, R., and J. B. Klemp, 1982: The influence of the shear-induced pressure gradient on thunderstorm motion. *Mon. Wea. Rev.,* **110,** 136–151.
——, and ——, 1985: On the rotation and propagation of simulated supercell thunderstorms. *J. Atmos. Sci.,* **42,** 271–292.
Rutledge, S. A., and P. V. Hobbs, 1984: The mesoscale and microscale structure and organization of clouds and precipitation in midlatitude cyclones. Part XII: A diagnostic modeling study of precipitation development in narrow cold-frontal rainbands. *J. Atmos. Sci.,* **41,** 2949–2972.
Straka, J. M., E. N. Rasmussen, and S. E. Fredrickson, 1996: A mobile mesonet for fine-scale meteorological observations. *J. Atmos. Oceanic Technol.,* **13,** 921–936.
Taylor, G. I., 1938: The spectrum of turbulence. *Proc. Roy. Soc. London,* **A164,** 476–490.
Taylor, J. R., 1982: *An Introduction to Error Analysis.* University Science Books, 327 pp.
Thompson, R. L., 1998: Eta Model storm-relative winds associated

with tornadic and nontornadic supercells. *Wea. Forecasting,* **13,** 125–137.
——, and R. Edwards, 2000: RUC-2 supercell proximity soundings. Part I: An examination of storm-relative winds normalized to supercell depth. Preprints, *20th Conf. on Severe Local Storms,* Orlando, FL, Amer. Meteor. Soc., 431–434.
Trapp, R. J., 1999: Observations of nontornadic low-level mesocyclones and attendant tornadogenesis failure during VORTEX. *Mon. Wea. Rev.,* **127,** 1693–1705.
——, E. D. Mitchell, G. A. Tipton, D. W. Effertz, A. I. Watson, D. L. Andra, and M. A. Magsig, 1999: Descending and nondescending tornadic vortex signatures detected by WSR-88Ds. *Wea. Forecasting,* **14,** 625–639.
U.S. Department of the Interior, 1992: *Standards for Digital Elevation Models.* U.S. Geological Survey National Mapping Division, 77 pp.
van Tassel, E. L., 1955: The North Platte Valley tornado outbreak of June 27, 1955. *Mon. Wea. Rev.,* **83,** 255–264.
Wakimoto, R. M., and C. Liu, 1998: The Garden City, Kansas, storm during VORTEX 95. Part II: The wall cloud and tornado. *Mon. Wea. Rev.,* **126,** 393–408.
——, and H. Cai, 2000: Analysis of a nontornadic storm during VORTEX 95. *Mon. Wea. Rev.,* **128,** 565–592.
——, C. Liu, and H. Cai, 1998: The Garden City, Kansas, storm during VORTEX 95. Part I: Overview of the storm life cycle and mesocyclogenesis. *Mon. Wea. Rev.,* **126,** 372–392.
Ward, N. B., 1961: Radar and surface observations of tornadoes of 4 May 1961. *Proc. Ninth Weather Radar Conf.,* Boston, MA, Amer. Meteor. Soc., 175–180.
Weisman, M. L., and J. B. Klemp, 1982: The dependence of numerically simulated convective storms on vertical wind shear and buoyancy. *Mon. Wea. Rev.,* **110,** 504–520.
Wicker, L. J., and R. B. Wilhelmson, 1995: Simulation and analysis of tornado development and decay within a three-dimensional supercell thunderstorm. *J. Atmos. Sci.,* **52,** 2675–2703.
Wilhelmson, R. B., and J. B. Klemp, 1978: A numerical study of storm splitting that leads to long-lived storms. *J. Atmos. Sci.,* **35,** 1974–1986.
Winn, W. P., S. J. Hunyady, and G. D. Aulich, 1999: Pressure at the ground in a large tornado. *J. Geophys. Res.,* **104,** 22 067–22 082.
Wurman, J., J. M. Straka, E. N. Rasmussen, M. Randall, and A. Zahrai, 1997: Design and deployment of a portable, pencil-beam, pulsed, 3-cm Doppler radar. *J. Atmos. Oceanic Technol.,* **14,** 1502–1512.